Topo-Bathymetric Lidar survey and analysis of the Stewiacke River, NS

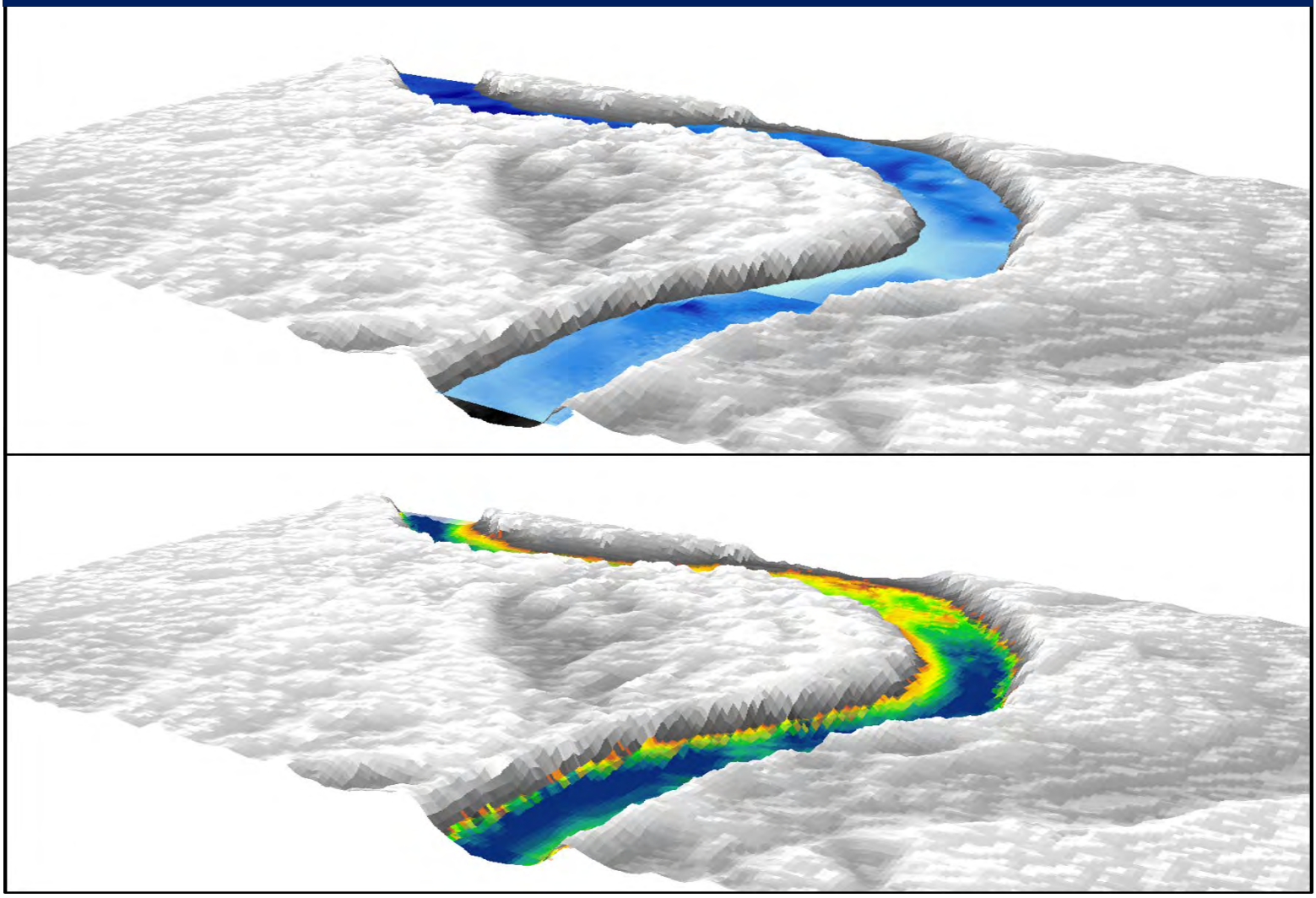

Prepared by

Applied Geomatics Research Group
NSCC, Middleton
Tel. 902 825 5475
email: tim.webster@nscc.ca

Submitted to

Stephen Williams
Fisheries Biologist
Department of Aquatic Resource and Fisheries Management. The Confederacy of Mainland Mi'kmaq

Webster, T., Ferris, K., McGuigan, K. Laskey, E. 2022. Topo-Bathymetric Lidar survey and analysis of the Stewiacke River, NS. Technical report, Applied Geomatics Research Group, NSCC Middleton, NS.

Copyright and Acknowledgement

The Applied Geomatics Research Group of the Nova Scotia Community College maintains full ownership of all data collected by equipment owned by NSCC and agrees to provide the end user who commissions the data collection a license to use the data for the purpose they were collected for upon written consent by AGRG-NSCC. The end user may make unlimited copies of the data for internal use; derive products from the data, release graphics and hardcopy with the copyright acknowledgement of **"Data acquired and processed by the Applied Geomatics Research Group, NSCC"**. Data acquired using this technology and the intellectual property (IP) associated with processing these data are owned by AGRG/NSCC and data will not be shared without permission of AGRG/NSCC.

Executive Summary

Topographic-bathymetric lidar (TB-lidar) systems typically utilize two lasers: a near infrared (NIR) laser for topographic data collection (land features and water surface) and a green laser for bathymetric data collection (seabed or river or lakebed). These systems generate high-resolution seamless digital elevation models (DEMs) that include land and submerged elevation. Most systems are equipped with a camera system, either a simple RGB or multispectral camera that can be utilized to generate coincident orthophoto mosaics from the same survey. There are shallow water TB-lidar systems that produce high density lidar points in water depths of 10s of centimeters to ca. 15 m depending on water clarity. The Applied Geomatics Research Group, AGRG- NSCC partnered with The Confederacy of Mainland Mi'kmaq (The CMM) and surveyed the Stewiacke River from its tidal influence with high turbidity to the upstream area near its headwaters with the Leica Chiroptera 4X airborne topo-bathymetric lidar sensor on a fixed-wing manned aircraft in the summer of 2021. The survey took two days to complete, Aug 1 and 18, with a few aborted flights in between because of low cloud cover and technical issues with the sensor that were resolved. In between survey flights the watershed experience rainfall events which elevated the water levels and increased turbidity throughout the river. Time was required to allow these conditions to subside before the flights could be finished. Several survey grade GNSS cross-sections were acquired across the river for validation. The river depth was calculated by subtracting the seamless (land-riverbed) elevation model from the water surface measured by the sensor. The inverse of the depth map (1/Depth) was used to calculate a cost surface for the river and a Least Cost path was constructed for the river where the path followed a course from deep pool to pool. From this line a Longitudinal Profile was extracted that can be used to assess fish passage and barriers. Efforts were made to classify the substrate of the river using a combination of the orthophotos captured with the lidar sensor and depth. This is still an active area of research to determine the limits of the sensor derived products.

Table of Contents

Executive Summary ii

Table of Contents iii

Table of Figures iv

1 Introduction 1

2 Methods 3

2.1 Sensor Specifications and Installation 3

2.2 Data Collection 3

2.3 Lidar Data Processing 7

2.4 Image Processing 12

2.5 Image Products 13

2.6 Lidar Products 14

2.7 Elevation and bathymetric height validation 14

2.8 Substrate Mapping 14

3 Results 17

4 Conclusion 28

Table of Figures

Figure 1 Topo-bathymetric lidar (TB-lidar) theory. A - Interaction of the NIR and green laser light when travelling between air and water, refraction and scattering take place. B - Typical elliptical scan patter for TB-LIDAR with navigation system GPS+IMU. C – Typical waveform captured from the green laser. (Source Leica) 2

Figure 2 Planned flight lines for Stewiacke River topo-bathymetric lidar survey. 3

Figure 3. Stewiacke River survey lines (aircraft trajectory) from Aug. 1 (black points/lines) and Aug. 18, 201 (red points/lines). 4

Figure 4 Environmental conditions around TB-lidar flights. A) Wind (quiver arrows direction and magnitude) and rain events (green) with St. Andrews River flow (blue) flight dates (red bars) for the date range July 29, Aug. 24, 2021. B) Aug 1 flight conditions. C) Aug 18 flight conditions. 5

Figure 5 Example of variable water clarity conditions Aug., 2021. A-B) Field photo of Stewiacke River showing visible submerged vegetation looking downstream. C) Orthophoto captured Aug. 18, 2021. D-E) Turbid water clarity conditions after Aug 2nd rain event, not the elevated water levels. F) Weather conditions and flights (red bars) and photo times (green bars). G-H) Clear but dark water Aug. 8 still at a high level after rain events Aug. 5-7. 6

Figure 6 Shaded relief of the seamless (land-riverbed) DEM of the Stewiacke River. 8

Figure 7 Example of how the river water depth is calculated. A) Shaded relief of the seamless DEM. B) Shaded relief DEM with water surface in blue. C) Shaded relief DEM with water depth (yellow to blue). D) View looking upstream of shaded relief with depth and transparent water surface (faint blue). 9

Figure 8 Example of the effect of bubbles on lidar depths. A) Orthophoto of rapids, white line shows beginning of rapids for reference. B) Water depth with white line as reference, note shortest path long profile line following deep pools. 10

Figure 9 Example of water depth derived from the topo-bathymetric lidar Aug. 18, 2021. A-B) Field photo of Stewiacke River earlier in August showing visible submerged vegetation looking downstream. C) Orthophoto captured Aug. 18, 2021. D-E) Turbid water clarity conditions after Aug 2nd rain event, not the elevated water levels. F) Weather conditions and flights (red bars) and photo times (green bars). G-H) Clear but dark water Aug. 8 still at a high level after rain events Aug. 5-7. 11

Figure 10 Example of the Longitudinal Profile generated by Least Cost Surface analysis on 1/Depth map, with start and end locations. Inset map to the upper left shows the depth and least cost path (ie. Long Profile) preferentially passing through deep pools. 12

Figure 11. True colour orthophoto mosaic Sections A-D of the Stewiacke River. 13

Figure 12. Colour shaded relief model of Section C of the study area with river depth overlaid. 14

Figure 13. Photo of Stewiacke River with AGRG researcher, Lauren Douglas, collecting survey grade GPS points. Photo on the right is a blow up of Lauren with GPS. 14

Figure 14 Approach to substrate classification. A) Orthophoto maps with orthophoto band ratio bottom index (orange to blue). B) Shaded relief with water depth (blue shades) and orthophoto band ratio bottom index (orange to blue). 16

Figure 15 The bottom classifications were determined from the Bottom Index Histogram (shown) while visually comparing the results with the air photo data. 17

Figure 16 Example of the 5 cm orthophotos acquired with river depth overlaid. Section A is where the river begins to be influences by the tide and turbidity levels increase. Section B is upstream from A and contains farmland adjacent to the river. Section C transitions from farmland into forest. Section D is upstream of C and is dominated by forest cover. 18

Figure 17 Example of colour shaded relief of seamless DEM with river depth. Section A is where the river begins to be influences by the tide and the gradient and floodplain and very broad and gently sloping. Section B is upstream from A and contains a broad floodplain with some moderate relief adjacent to the river. Section C transitions from broad floodplain to a narrower valley with higher adjacent relief. Section D is upstream of C and has the highest relief although the floodplain is less pronounced that Section C. 19

Figure 18 Example of the Least Cost Path (white line) overlaid on river depth (orange to blue- deepest) and colour shaded relief DEM. 20

Figure 19 Longitudinal profile of Stewiacke River. Orange line is the water surface, and the blue line is the riverbed. 21

Figure 20 Close up of the long profile from upstream distance 1000 m to 3000 m. The orange line is the water surface and the blue line is the river bed. 21

Figure 21 Histogram and statistics of the difference in elevation between the GPS points and the DEM along roads. The mean DZ (GPS-DEM) is -2 cm with a standard deviation of 4 cm. 22

Figure 22. GPS validation of riverbed bathymetry. A) Location of transect #1. B) Graph of GPS (black) and lidar DEM (blue) with difference (GPS-DEM) in red. 23

Figure 23. GPS validation of riverbed bathymetry. A) Location of transect #2. B) Graph of GPS (black) and lidar DEM (blue) with difference (GPS-DEM) in red. 24

Figure 24 Example of riverbed substrate mapping. The extent of this figure is similar to that of figure 18. A) Orthophoto of river bend. B) Orthophoto with water depth. C) Substrate map of river bend. 26

Figure 25 Another example of substrate mapping of Stewiacke Riverbed upstream of figure 24. A) Orthophoto map. B) Substrate map over orthophoto. 27

1 Introduction

Topo-bathymetric lidar works by emitting a near-infrared (NIR) and a green laser from an aircraft, typically in an elliptical or circular scan pattern, and measuring the travel time of the laser pulses to and from the land, water surface, and seabed (Figure 1-A, B). The NIR laser pulse reflects off the land or water, while some of the green laser pulse is reflected at the air-water interface and the rest is refracted and attenuated as it passes through the water column and reflected from the seabed to return to the detector (Figure 1-C). The travel path of the green laser is complex as it passes from air to water the speed of the light slows down by approximately 1/3 and thus is refracted. Once in the water column, the green light is scattered and losses its energy exponentially with depth until it reflects off the sea-river bed and returns to the detector. In order to compensate for the refraction angle and change in the speed of light from air to water, the system must be able to detect the water surface. The NIR laser returns and the green laser returns are used to detect the water surface in order to compensate for these optical path effects of the green laser changing media from air to water and the return path back to the detector. The beam divergence of the NIR laser is typical of that of topographic lidars on the order of 0.5 mrad whereas the green laser will have a larger beam divergence at 3 mrad.

Unlike sonar, where the speed of sound in water is significantly affected by salinity and temperature, TB-lidar works equally well in fresh or saltwater. However, the water clarity is typically the limiting factor for a successful TB-lidar survey. The reflectance of seabed or river-lakebed also plays a role in addition to water clarity for determining how deep the green laser can penetrate and reflect back to the sensor.

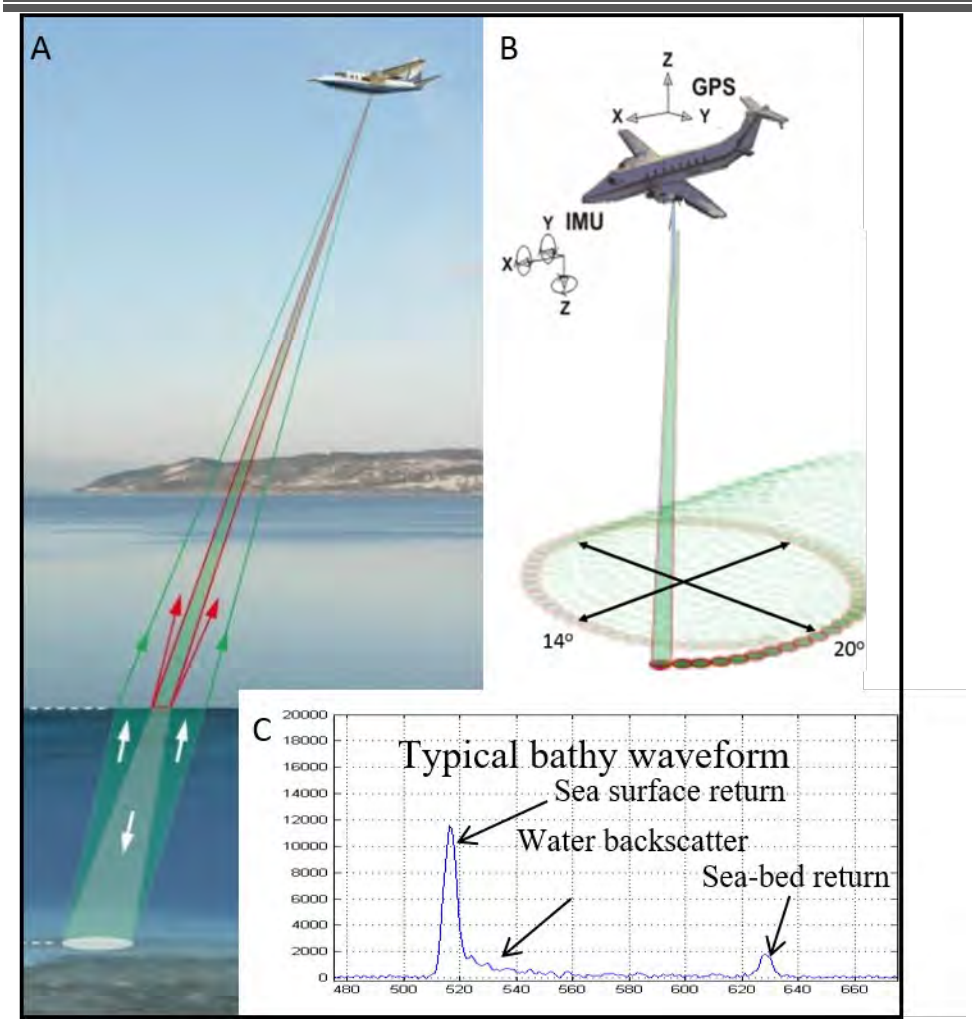

Figure 1 Topo-bathymetric lidar (TB-lidar) theory. A - Interaction of the NIR and green laser light when travelling between air and water, refraction and scattering take place. B - Typical elliptical scan patter for TB-LIDAR with navigation system GPS+IMU. C – Typical waveform captured from the green laser. (Source Leica)

The Nova Scotia Community College – Applied Geomatics Research Group (NSCC-AGRG) own and operate a Leica Chiroptera 4X (CH4X) high-resolution topo-bathymetric lidar scanner equipped with an ancillary Leica RCD30 60-megapixel multispectral (RGB-Nir) camera that can survey seabed morphology and habitat, including submerged vegetation (Webster et al., 2019). More recently AGRG has been conducting surveys over rivers to test the applicability of the sensor to provide riverbed depth and morphology that can aid in fish passage and fish habitat studies.

2 Methods

Methods on survey preparation, sensor management, field sampling and data processing are detailed in the following sections.

2.1 Sensor Specifications and Installation

The lidar sensor used in this survey was the Leica Chiroptera 4X integrated topographic-bathymetric lidar sensor equipped with a 60-megapixel Leica RCD30 multispectral (RGB-Nir) camera. The lidar uses a 1064 nm near-infrared laser to survey ground and sea surface positions at 500 kHz and a green 515 nm laser to survey bathymetric positions at 35 kHz. The lasers scan in an elliptical pattern, which facilitates coverage from many different angles on vertical faces, produces fewer shadow effects in the data, and is less sensitive to wave interaction when compared to lateral 'saw tooth' scanners. The ability of the bathymetric laser to penetrate the water column is limited by water clarity. The system has a depth penetration rating of roughly 1.5 x visible extinction (Secchi depth). The Leica RCD30 camera collects coincident multispectral motion compensated imagery. NSCC-AGRG partnered with Leading Edge Geomatics (LEG) to charter a Piper Navajo twin engine aircraft capable of housing the lidar unit. The CH4X was installed in the aircraft in Debert, NS on July 27, 2021, and calibrated on July 28, 2021, over a ground control site established by NSCC-AGRG in Truro.

2.2 Data Collection

Survey lines were planned using Leica Mission Pro at 400 m altitude at a speed of 65 m/s with 30% lateral overlap to ensure that no data gaps (Figure 2). The flight originated from the Debert airport and part of the study area

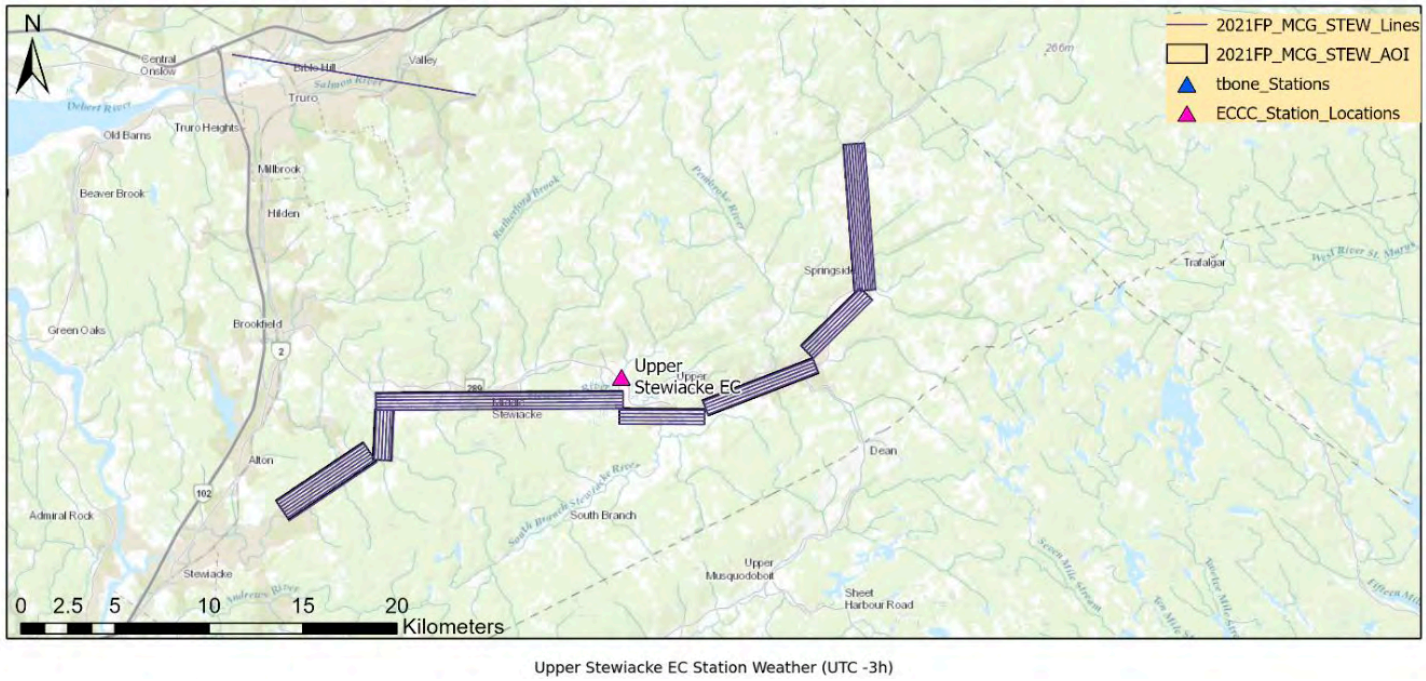

Figure 2 Planned flight lines for Stewiacke River topo-bathymetric lidar survey.

was surveyed on August 1 and the remainder of the area was surveyed on August 18, 2021. The activity control station at Bible Hill/Truro was used for the GNSS base station (Figure 3).

We monitored the weather as well as a flow gauge for water levels on the nearest stream to the Stewiacke River, which is the St. Andrews River.

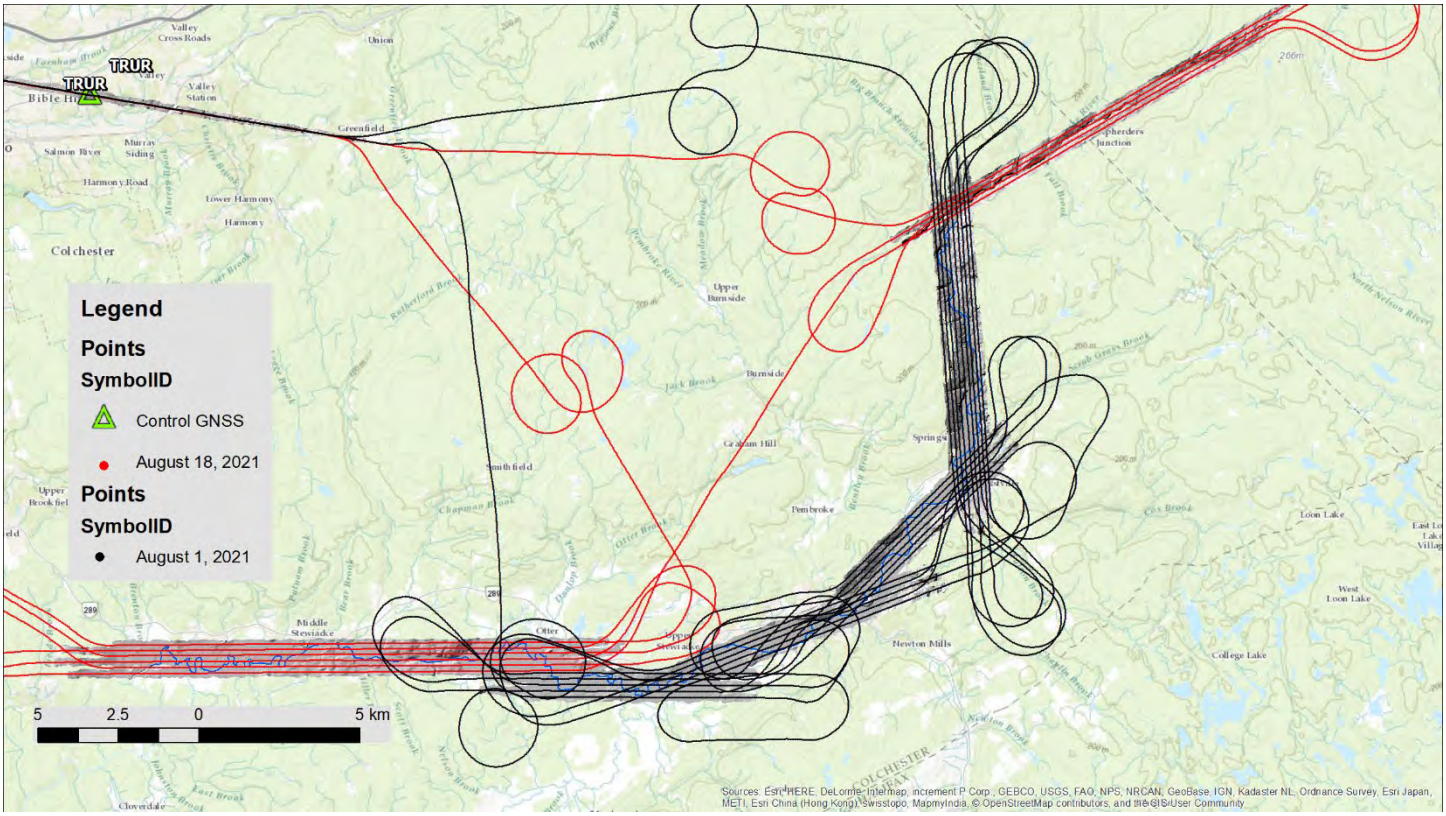

Figure 3. Stewiacke River survey lines (aircraft trajectory) from Aug. 1 (black points/lines) and Aug. 18, 201 (red points/lines).

Figure 4 Environmental conditions around TB-lidar flights. A) Wind (quiver arrows direction and magnitude) and rain events (green) with St. Andrews River flow (blue) flight dates (red bars) for the date range July 29, Aug. 24, 2021. B) Aug 1 flight conditions. C) Aug 18 flight conditions.

The site was visited quite frequently in order to determine the water clarity conditions which directly affect the laser's ability to penetrate the water column. Below are examples of how the depth and water clarity change in reaction to rain and storm events (Figure 5).

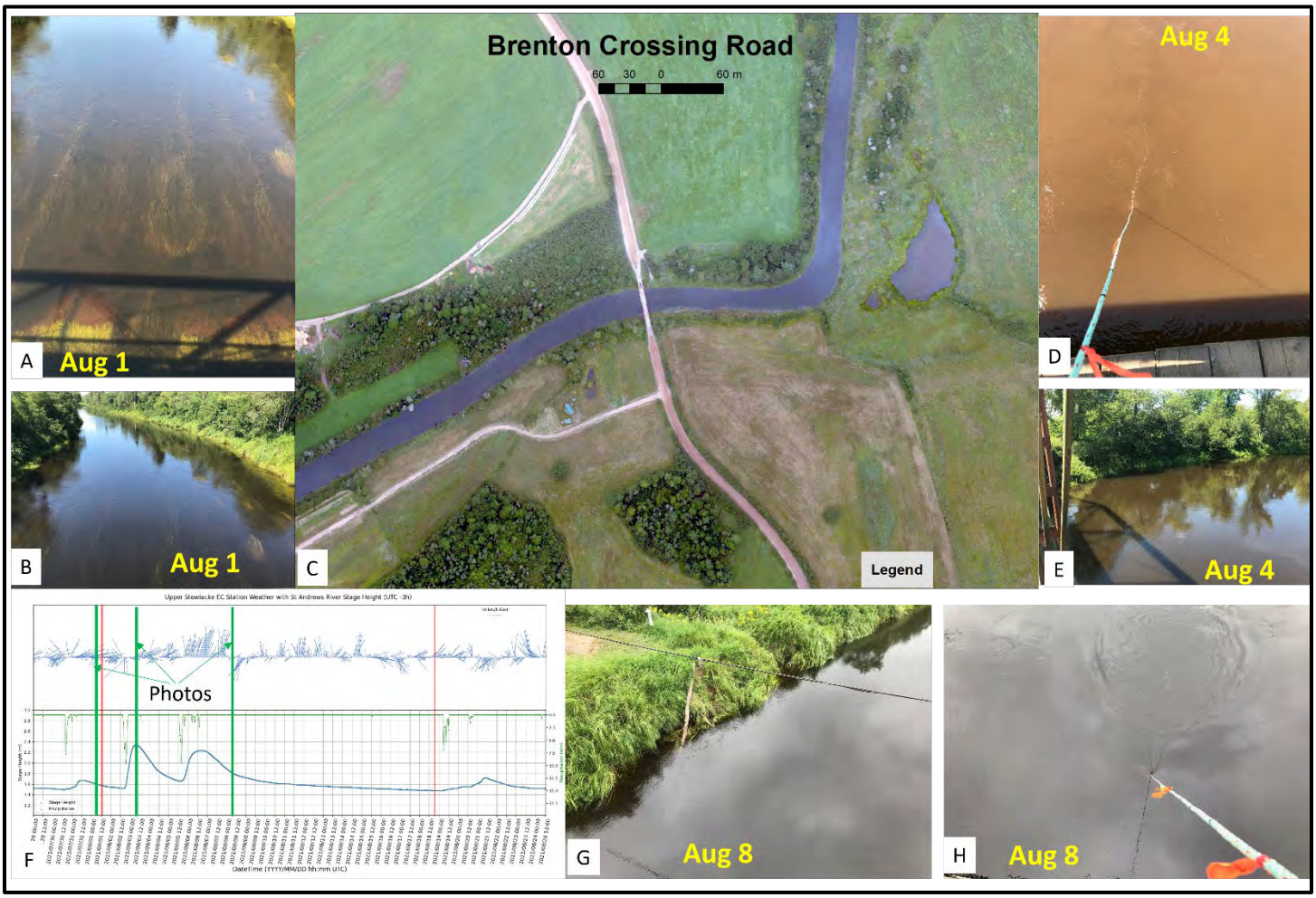

Figure 5 Example of variable water clarity conditions Aug., 2021. A-B) Field photo of Stewiacke River showing visible submerged vegetation looking downstream. C) Orthophoto captured Aug. 18, 2021. D-E) Turbid water clarity conditions after Aug 2nd rain event, not the elevated water levels. F) Weather conditions and flights (red bars) and photo times (green bars). G-H) Clear but dark water Aug. 8 still at a high level after rain events Aug. 5-7.

2.3 Lidar Data Processing

A smoothed trajectory of the lidar and camera positions was calculated by linking system GNSS positions and IMU attitude with the control data from nearby stations using NovAtel Inertial Explorer. Leica Lidar Survey Studio (LSS) was used to process Chiroptera 4X waveforms to discrete georeferenced (NAD83 CSRSv7) points by linking laser returns to the processed aircraft trajectory to produce point clouds in the LAS format. The data were inspected to ensure there was sufficient overlap (30%) and the AOI was fully covered by lidar returns. LAS files were read into Bentley TerraScan to analyze and further refine point metrics. Points were classified into discrete classes based on their physical characteristics including relative geometry and reflective properties (Table 1).

Table 1. Lidar point classification values and descriptions

Classification Value	Meaning
1	Unclassified
2	Ground
4	Medium vegetation
7	Low point (noise)
9	Topographic water surface
18	High noise
40	Bathymetric point
41	Bathymetric water surface
42	Derived water surface
80	Bathymetric vegetation

Three data products were derived directly from the lidar point cloud, 1) a rasterized digital elevation model (DEM) that included only returns that were classified as ground above and below the water line, and 2) a rasterized digital surface model (DSM) that included all lidar points, and 3) a rasterized model of laser return intensities. Lidar return intensity is influenced by several factors including the local angle of incidence with the target, the natural reflectivity of the target material, the voltage or gain of the transmitted lidar pulse, and attenuation of the energy within the water column. Raw reflectance data are difficult to interpret due to these covariances and normalized values are needed to isolate the natural reflectivity of the target. A process has been developed to normalize the amplitude data for signal loss in a recent publication (Webster et al., 2016). The bare-earth DEM was shaded to highlight where the Stewiacke River was surveyed (Figure 6).

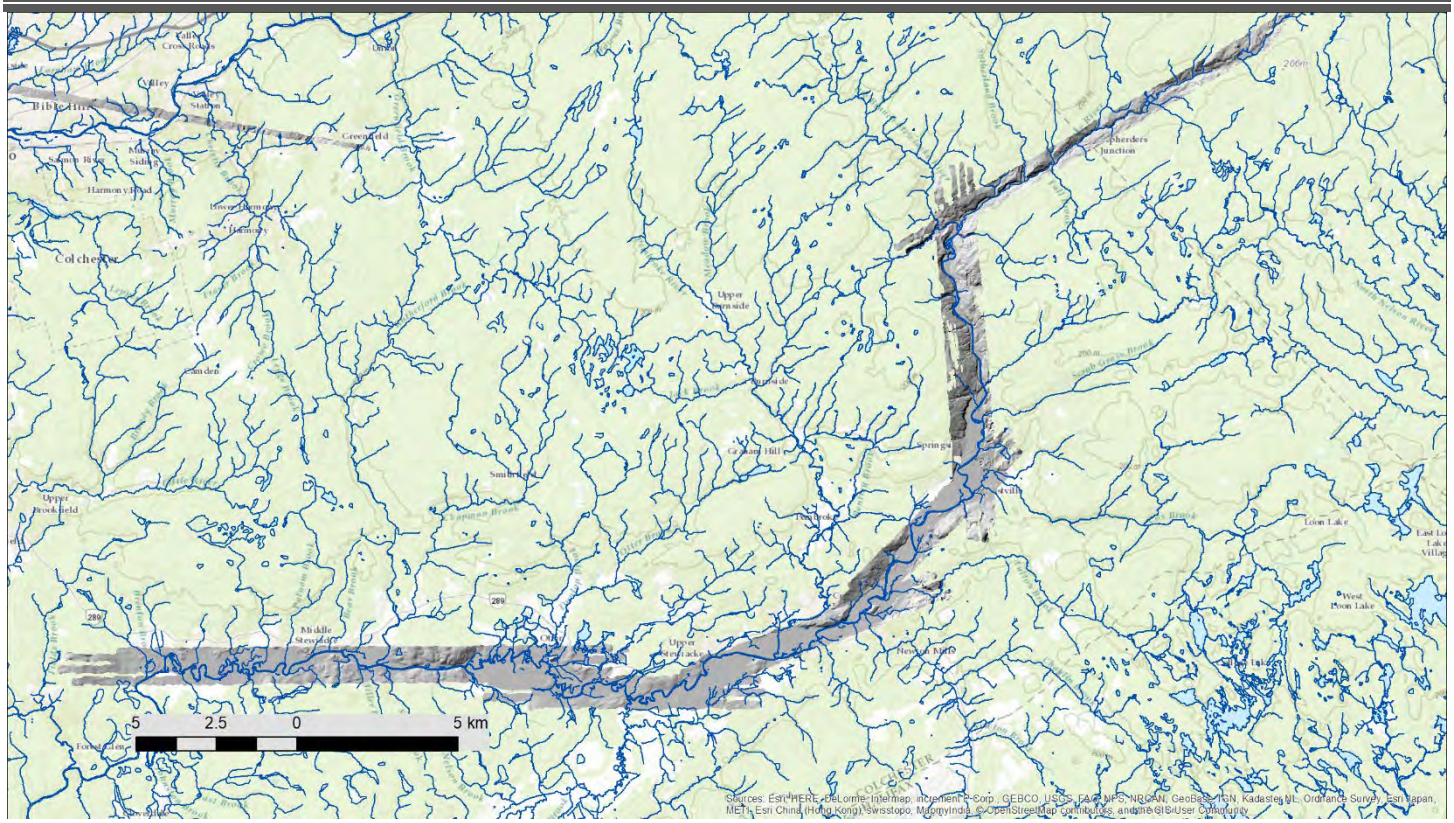

Figure 6 Shaded relief of the seamless (land-riverbed) DEM of the Stewiacke River.

The TB-lidar sensor measures the water surface using both the green laser returns and the NIR laser returns. From these two sets of data a "modelled" water surface is derived that is used to calculate the refraction angle and change of speed of light when passing from air into water and then on the reverse path back to the sensor. The derived water surface was not perfect and contained both omission and commission errors, meaning it missed some of the water where the stream was quite small and in rare cases put water surface in land areas. The water surface was cleaned, and the errors fixed using GIS selection techniques. Once a suitable water surface was derived, the elevations of the water surface were subtracted from the DEM surface to construct a water depth map (Figure 7).

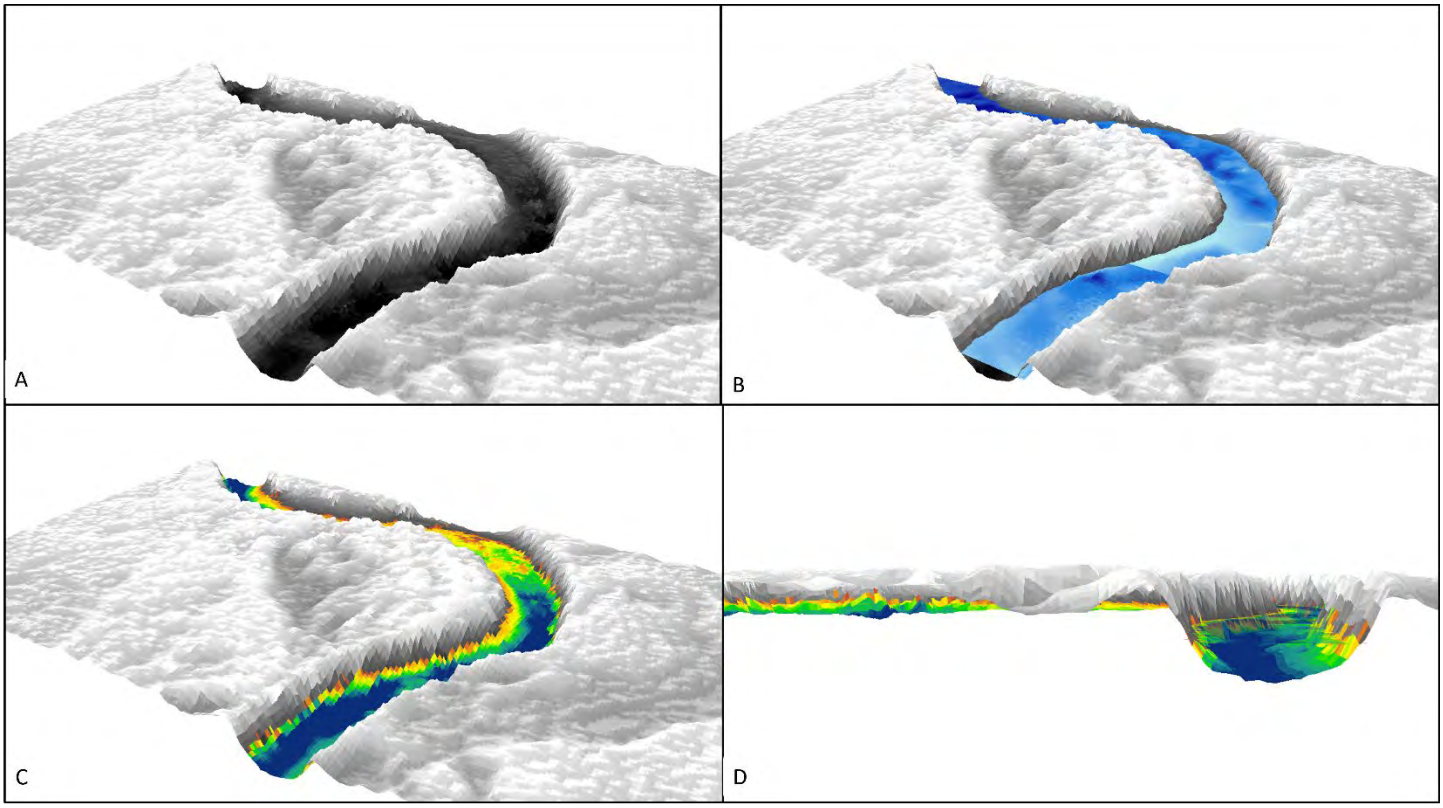

Figure 7 Example of how the river water depth is calculated. A) Shaded relief of the seamless DEM. B) Shaded relief DEM with water surface in blue. C) Shaded relief DEM with water depth (yellow to blue). D) View looking upstream of shaded relief with depth and transparent water surface (faint blue).

Once the water depth map was made it was inspected for artifacts. There were two types of errors detected in the water depth map: 1) areas that appear to be too deep (> 1.7 m) for any green laser returns, and 2) areas where bubbles after rapids impeded the green laser from reaching the riverbed (Figure 8). In the figure below the depths are accurate before the area of rapids where the riverbed shallows up (white line on figure), however the shallow depths are judged not to be accurate downstream of the rapids as a result of the bubbles and foam generated. The depths shown as orange colours downstream reflect the surface elevation where the lidar could not penetrate through the bubbles to the riverbed (Figure 8).

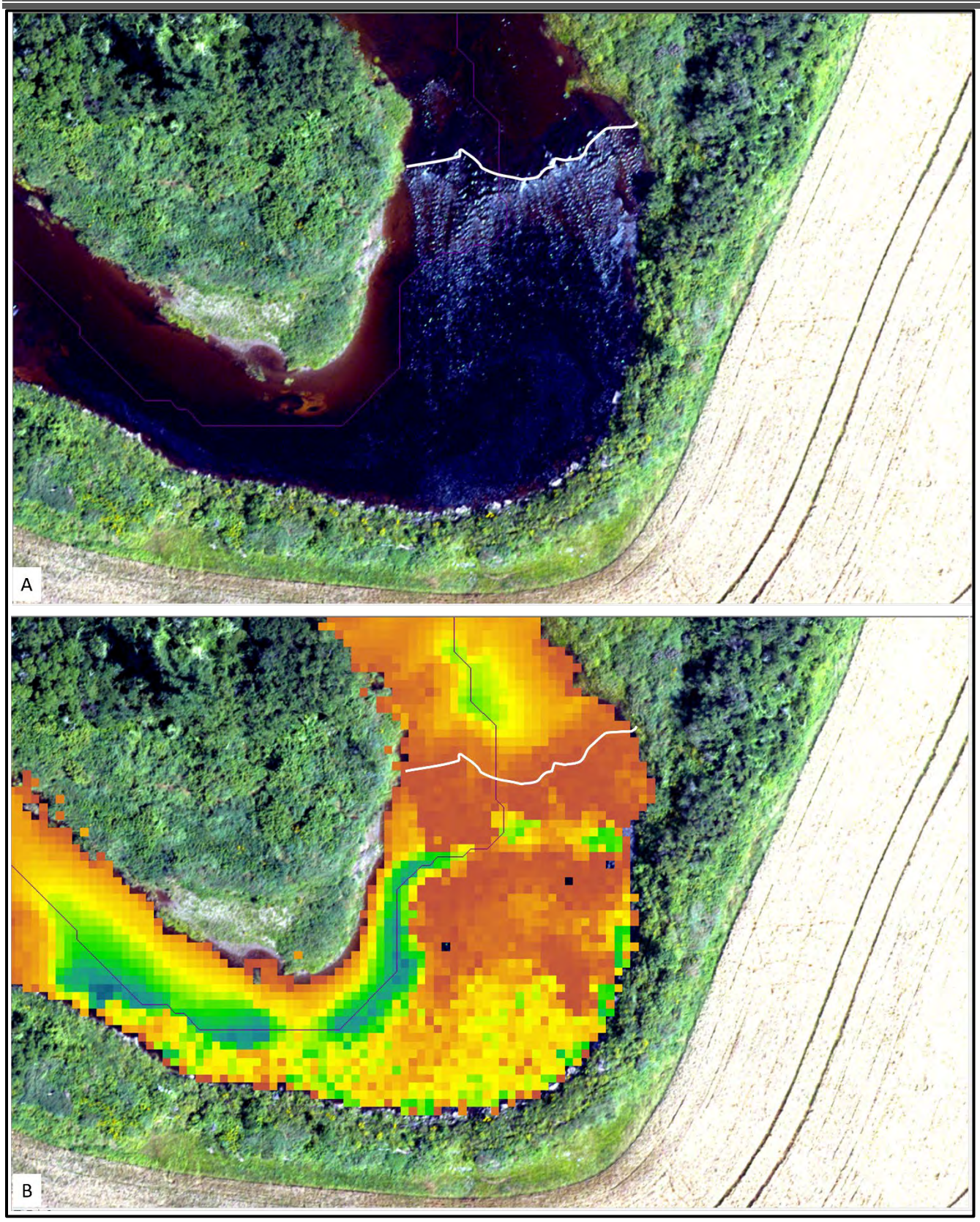

Figure 8 Example of the effect of bubbles on lidar depths. A) Orthophoto of rapids, white line shows beginning of rapids for reference. B) Water depth with white line as reference, note shortest path long profile line following deep pools.

Other areas that have questionable depths are where bridges crossed the river and obstructed the green laser's ability to penetrate to the bottom (Figure 9).

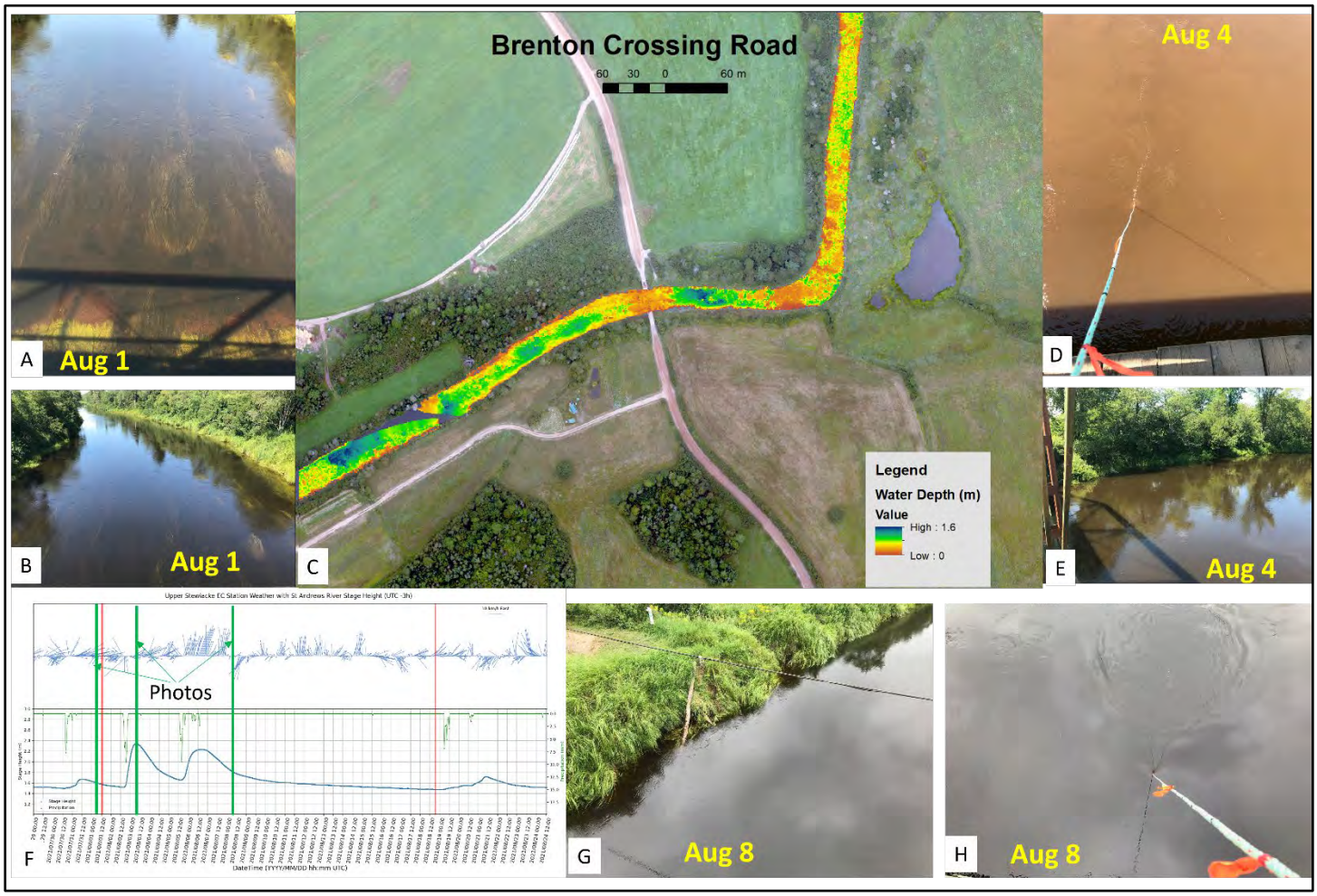

Figure 9 Example of water depth derived from the topo-bathymetric lidar Aug. 18, 2021. A-B) Field photo of Stewiacke River earlier in August showing visible submerged vegetation looking downstream. C) Orthophoto captured Aug. 18, 2021. D-E) Turbid water clarity conditions after Aug 2nd rain event, not the elevated water levels. F) Weather conditions and flights (red bars) and photo times (green bars). G-H) Clear but dark water Aug. 8 still at a high level after rain events Aug. 5-7.

A start and end point were digitized along the main stretch of the river where continuous depth measurements were resolved. The GIS Least Cost Connectivity Analysis was then executed to derive a single line representing the path of least resistance from the start to the end location. The cost surface was the inverse of the depth map, calculated as 1/Depth, thus deep areas would have a low cost and shallow areas a higher cost (Figure 10).

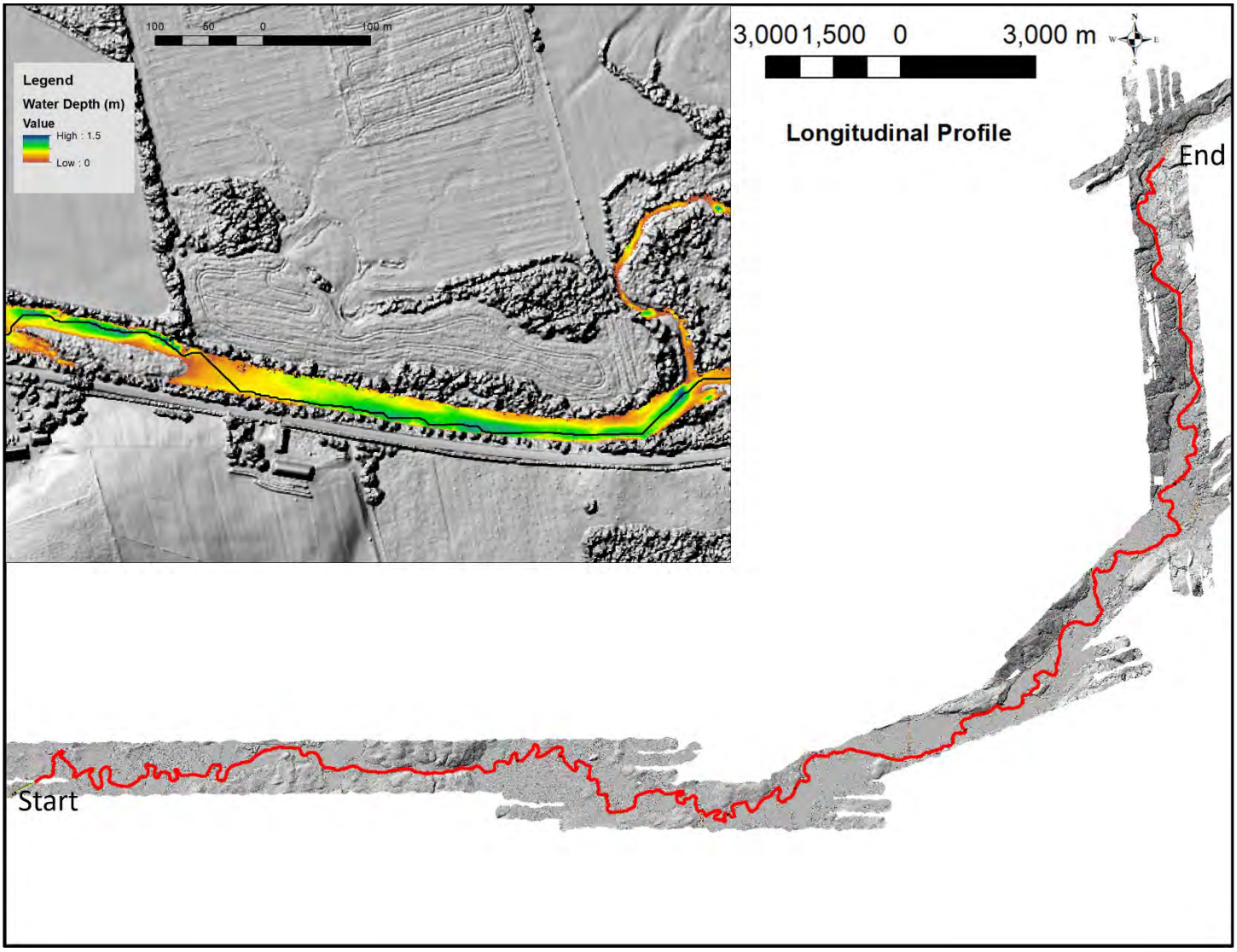

Figure 10 Example of the Longitudinal Profile generated by Least Cost Surface analysis on 1/Depth map, with start and end locations. Inset map to the upper left shows the depth and least cost path (ie. Long Profile) preferentially passing through deep pools.

Once the seamless DEM and DSM were constructed a colour shaded relief map was constructed for the survey area they can be used to interpret the relief in the area.

2.4 Image Processing

Multispectral RCD30 imagery was processed using Agisoft Metashape Professional. The processed smooth trajectory was linked to image events based on system time tags. This linkage was used to define the exterior orientation (EO) for each of the RCD30 images where camera position (x, y, z) and attitude (yaw, pitch, roll; omega, phi, kappa) were recorded for

every exposure with positional accuracies better than 0.01 m and rotational accuracies better than 0.004 degrees. Any ambiguity between relief displacement and lens distortion was solved using by generating a well-defined internal orientation (IO) of the engineered zero distortion RCD30 lens during the camera boresight process at the Truro calibration site. Captured imagery was positioned using an aerial triangulation model where possible to generate the best relief map for subsequent orthorectification. Where photo positions were unable to be resolved, such as deep open water with few image tie-points, imagery was directly georeferenced using the EO and IO.

2.5 Image Products

The orthophoto mosaic product was generated at a resolution of 0.05 m resolution with pixel perfect alignment between frames and covered the entire extent of the AOI. The initial mosaic was very large, considering the pixels are at 5 cm resolution and the river study area is quite convoluted. The orthophoto mosaic was broken up into four distinct parts: Section A, B, C, and D to allow easier access and interaction with the data (Figure 11). False colour composite imagery which incorporated the near-infrared band was found to be suitable for mapping vegetation in the region.

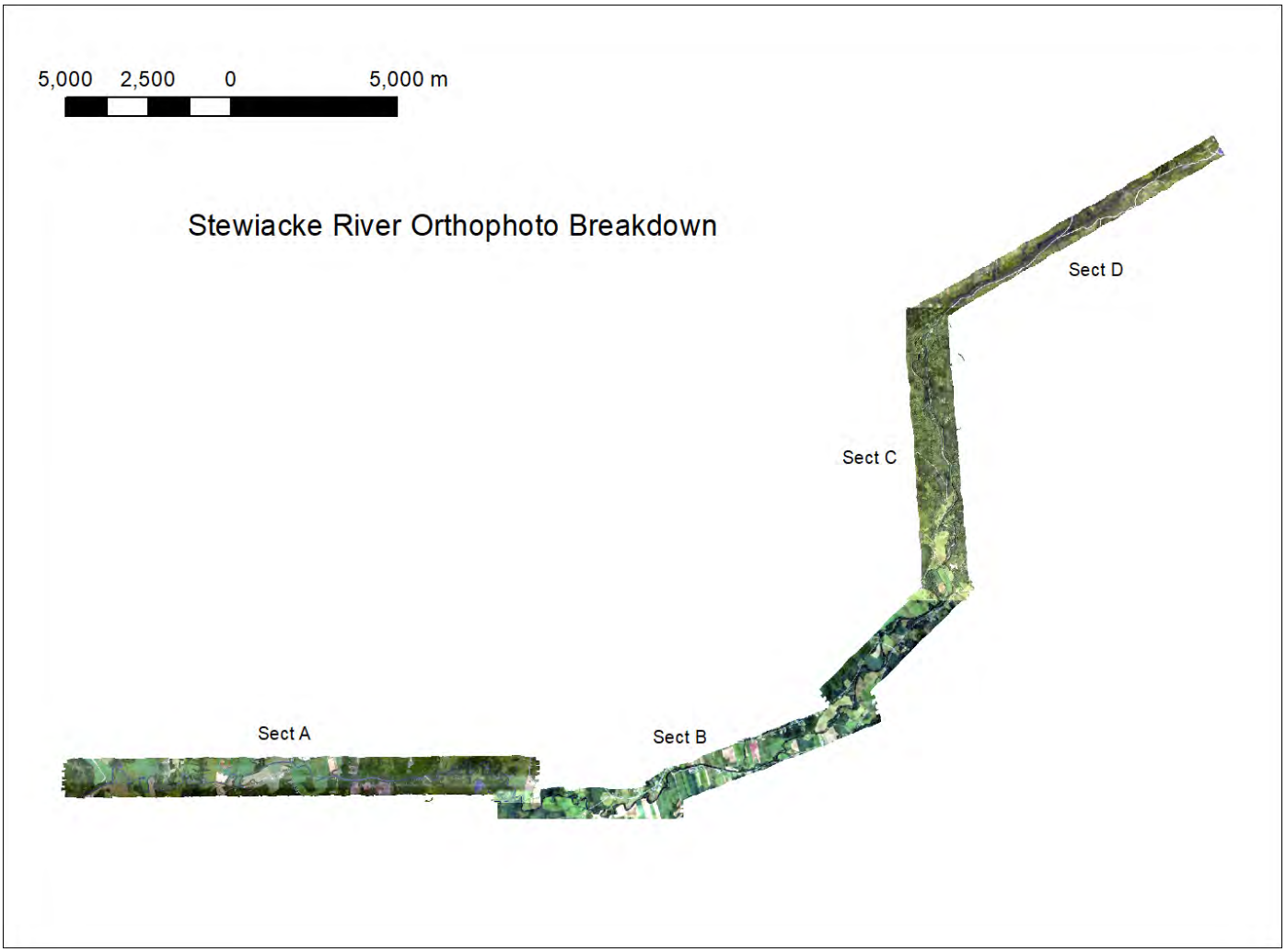

Figure 11. True colour orthophoto mosaic Sections A-D of the Stewiacke River.

2.6 Lidar Products

Topographic and bathymetric data were of high quality and exhibited very little noise which resulted in smooth elevation models and colour shaded relief models that combine elevation information from the DEM with a colour ramp to highlight differences in elevation (Figure 12).

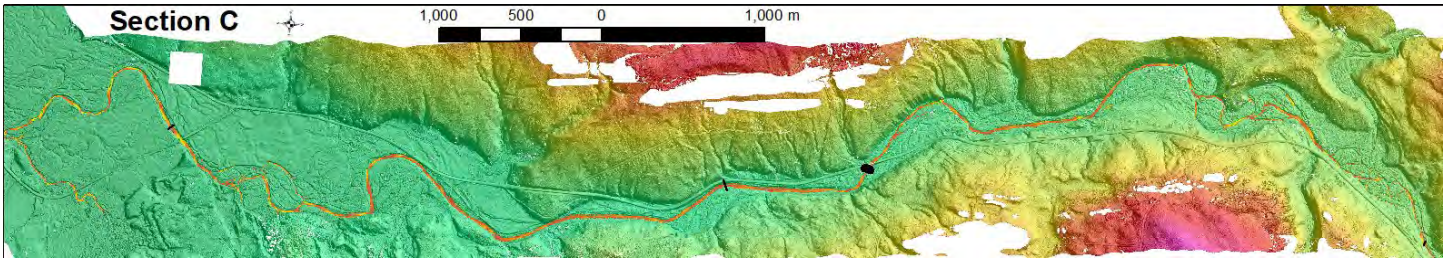

Figure 12. Colour shaded relief model of Section C of the study area with river depth overlaid.

2.7 Elevation and bathymetric height validation

In order to validate and check the elevations collected by the lidar, we collected survey grade (2-5 cm vertical precision) GPS data along the roads near bridges and along and across the riverbed where possible (Figure 13).

Figure 13. Photo of Stewiacke River with AGRG researcher, Lauren Douglas, collecting survey grade GPS points. Photo on the right is a blow up of Lauren with GPS.

The GPS points were separated into points along the road, “hard points” to test the topographic lidar returns and river transect points to test the bathymetric lidar return accuracy.

2.8 Substrate Mapping

We utilized the river depth and orthophoto bands to attempt to classify the river substrate material. The RGB and NIR bands of the RCD30 camera produce high resolution orthophotos at 5 cm compared to the lidar elevation and intensity

models at 1 m. Various band ratios were calculated (Bx-By)/(Bx+By) which has a tendency to normalize various in the photos caused by shadows and or sun glint (Figure 14). The band ratios were combined with depth to attempt to resolve the substrate signal through the water column. The dark water makes this very difficult as the reflected signal from the substrate is very faint and lacks strong contrasts between substrate types. This approach proved to be very challenging and will require more time for image processing experimentation and the collection of more in-situ ground truth data on substrate.

Normalizing difference ratios are well established as a metric for auto normalizing radiometric data to various atmospheric conditions. In the water column, these ratios provide the added benefit of adjusting the exponentially decaying signals of red, green, and blue light (as observed by the RCD30 camera) to a simple linear relationship with depth. Simply utilizing the sum of various permutations of these colors the radiometric signal can be increased throughout the water column. Furthermore, by subtracting a ratio derived from the non-penetrating near infrared channel (NIR), surface effects such as non-specular glint can be reduced. By observing the output, a reasonable threshold range can be set to capture the available signal visible through the water column, represented in the following equation:

$$Color_{index} = 0.1 < \frac{Red - Green}{Red + Green} + \frac{Green - Blue}{Green + Blue} + \frac{Blue - Red}{Blue + Red} - \frac{Blue - NIR}{Blue + NIR} < 0.5$$

To compensate for the linear decay of the above index, the modelled lidar water surface is used to calculate depth of the lidar bathymetric raster. This depth measure is truncated beyond 2 meters depth where the visible signal has become significantly attenuated. This value is tuned specifically to the water conditions.

$$Depth_{index} = 0 < Water_Z - RiverBathymetry_z < 2.0$$

Both above indexes are re-normalized from 0 to 1 (i.e., stretched from 0.1 – 0.5 range to an output of 0 – 1 range) such that a simple sum can compensate for the linear decay with increased water depth.

$$Bottom_{index} = Color_{index} + Depth_{index}$$

This resulting metric contains the sum of the normalized color data from the RCD30 camera system which has been corrected for the linear attenuation with depth. Thus, the result is a single index reflecting the bottom reflectance across multiple spectral bands which has been decoupled from the depth of the water column. Hence this metric is intended to represent the radiometry of the river bottom (Figure 15).

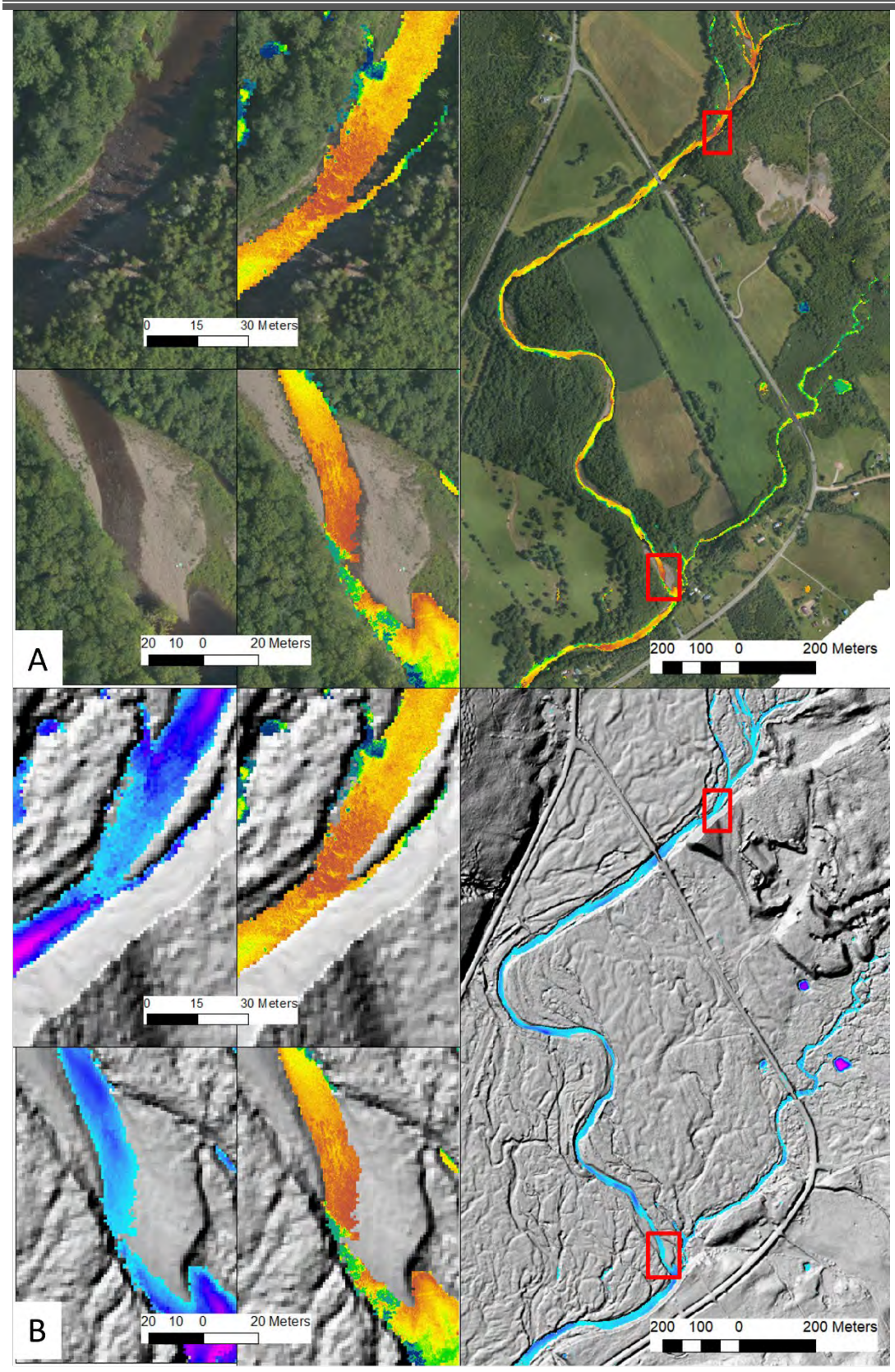

Figure 14 Approach to substrate classification. A) Orthophoto maps with orthophoto band ratio bottom index (orange to blue). B) Shaded relief with water depth (blue shades) and orthophoto band ratio bottom index (orange to blue).

The single index was then inspected to manually threshold and provide insight into the varying bottom characteristics of the river. In this case, it was observed in air photo analysis that lower index values matched well systematically with coarser pebbly substrate, whereas what were interpreted as softer sediments trended toward higher index values. Values greater than 1 tended to strongly represent vegetation overhanging the river – where the NIR component of the *Color Index* is strongly positive.

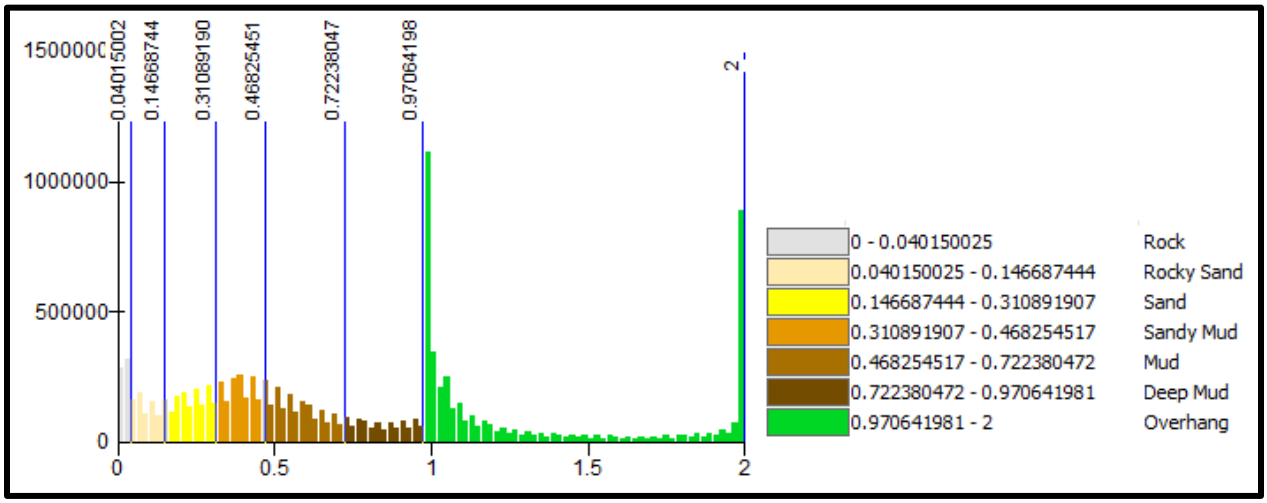

Figure 15 The bottom classifications were determined from the Bottom Index Histogram (shown) while visually comparing the results with the air photo data.

Note that this analysis does presume that water column conditions are relatively stable throughout the river. It was observed that the effect of decoupling this *Bottom Index* from the water column was highly successful in the upper shallow portions of the river specifically, where the bottom types as depicted are not highly correlated to water depth. Further downstream the correlation does markedly increase though this relationship is certainly real to some extent as softer sediments would accumulate in deeper lower energy pools along the river bottom.

3 Results

The results of the topo-bathymetric lidar survey for the Stewiacke River are impressive, given the size and length of the area surveyed and the challenging environmental conditions that were occurring during the survey period. As mentioned, the study area is quite large and has a convoluted shape, thus the orthophoto maps were broken into four sections to facilitate quicker access and loading of the imagery in GIS (Figure 16).

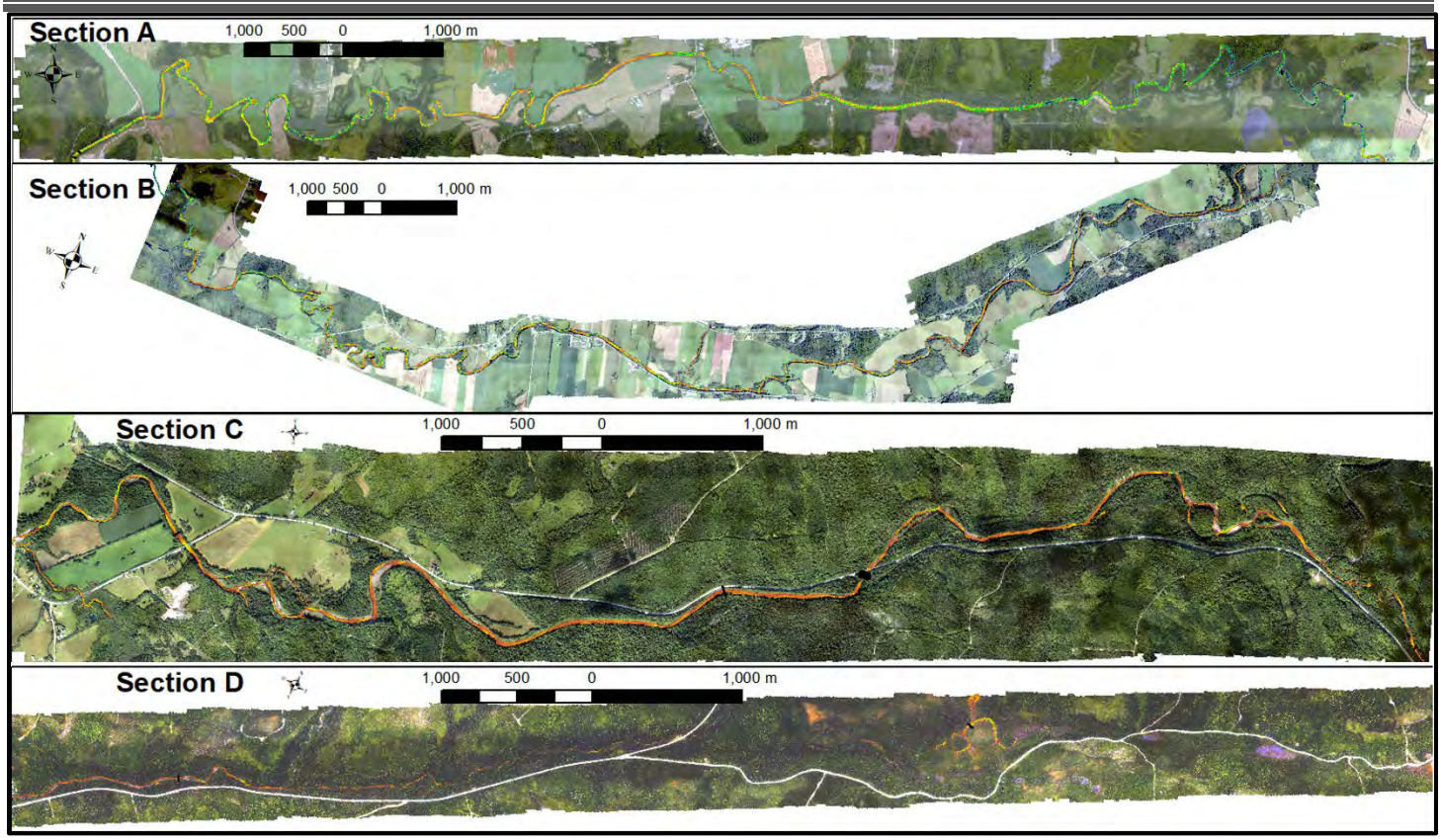

Figure 16 Example of the 5 cm orthophotos acquired with river depth overlaid. Section A is where the river begins to be influences by the tide and turbidity levels increase. Section B is upstream from A and contains farmland adjacent to the river. Section C transitions from farmland into forest. Section D is upstream of C and is dominated by forest cover.

The lidar surface models DSM and DEM where processed as one large colour shaded relief map but have been displayed at the same scale and extent as figure 16 to compare the relief with the orthophotos using the DEM (Figure 17).

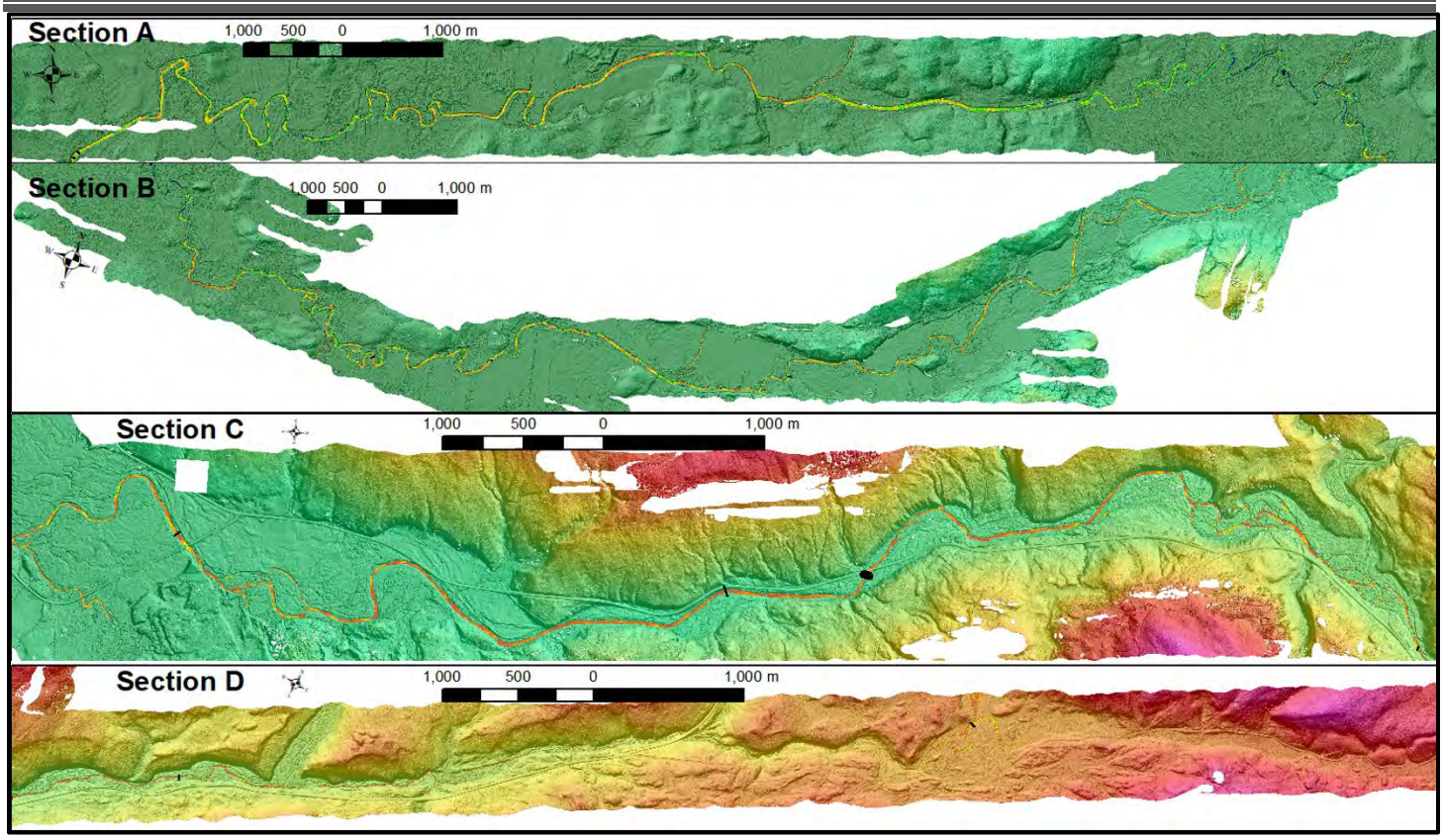

Figure 17 Example of colour shaded relief of seamless DEM with river depth. Section A is where the river begins to be influences by the tide and the gradient and floodplain and very broad and gently sloping. Section B is upstream from A and contains a broad floodplain with some moderate relief adjacent to the river. Section C transitions from broad floodplain to a narrower valley with higher adjacent relief. Section D is upstream of C and has the highest relief although the floodplain is less pronounced that Section C.

As described in the methods, the river depth was calculated using a combination of the water surface and seamless DEM (Figure 18). Note how the path (white line Figure 18) selectively passes through the deep pools. This method attempts to map a possible path fish would use as passage through the river system where they would preferentially swim from pool to pool (Figure 18). Another advantage of this least cost path is that is does not meander back and forth between the shores across the channel, and thus would represent too large of length for the river. This issue has been demonstrated using topographic lidar with the results of the stream defined by GIS watershed tools. In this case, however the path is the shortest distance along the channel and ensures it passes from one pool to the next (Figure 18). This results in a more accurate representation of the true river length and has the benefit of mapping the pools along the longitudinal profile (Figure 19).

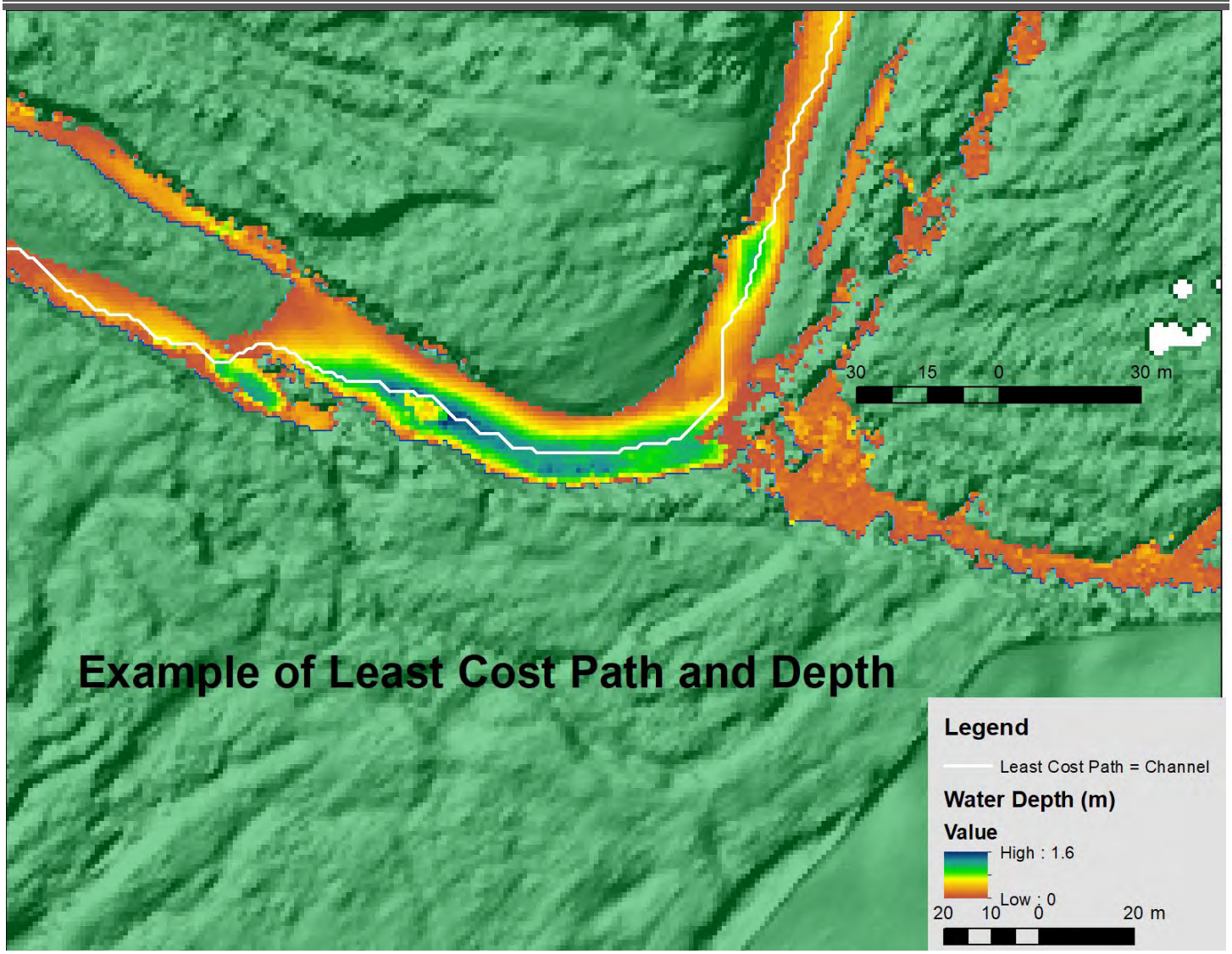

Figure 18 Example of the Least Cost Path (white line) overlaid on river depth (orange to blue- deepest) and colour shaded relief DEM.

From these data a cost surface was calculated simply by taking the inverse of depth (1/Depth) to be used as the cost surface. This was used to calculate the least cost path from the start to end point along the river. Once the least path line was calculated, it was split into points every 1 m along the line and the water surface and DEM elevations were appended to it. From these data a longitudinal profile was constructed that included the water surface and riverbed (Figure 19, Figure 20). Note how the longitudinal (long) profile changes from a very steep gradient in the upstream section to nearly flat from 12,000 to 25,000 m upstream distance and then steps down approximately 5 m from upstream distance 12,000 to ~ 5,000 m and is flat again for the remainder (Figure 19). The elevation ranges from ~85 m in the upstream section to ~ 10 m downstream over a distance of ~ 55 km (Figure 19). The close up of the long profile shows the location of pools (blue line far below the orange, Figure 20) and rifles where the blue line is close to the orange line. This close up is near the end of the profile where the river flattens along its path.

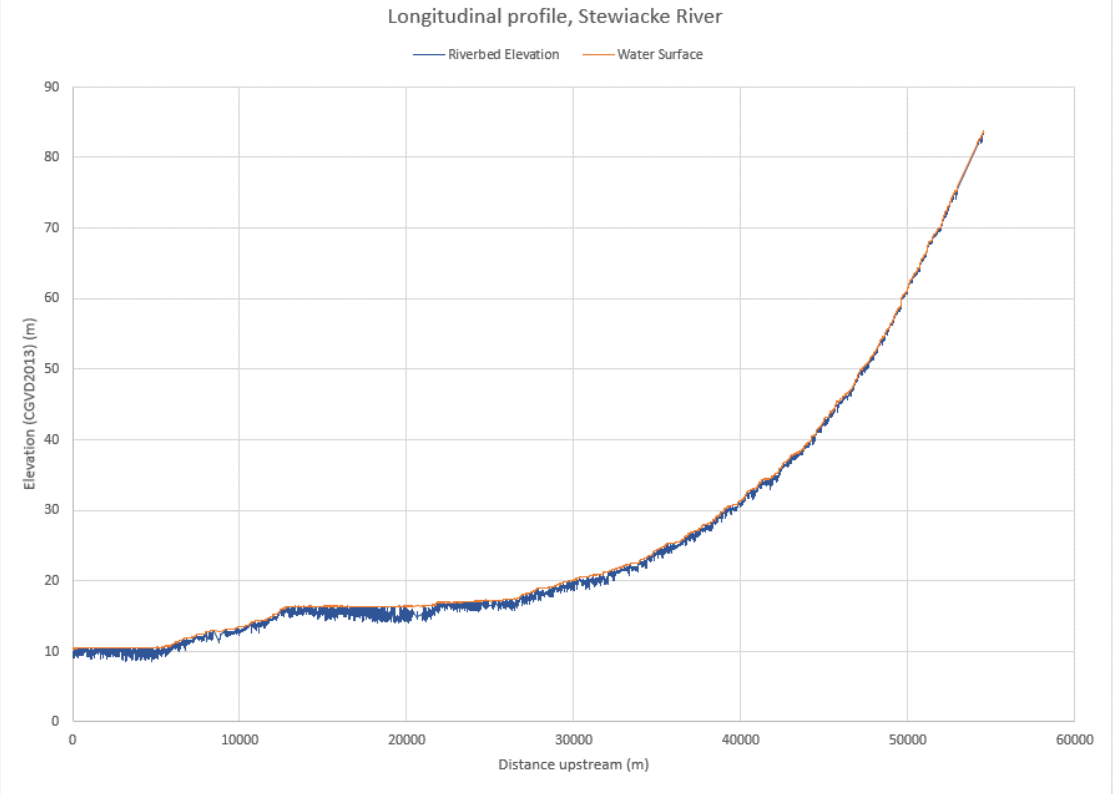

Figure 19 Longitudinal profile of Stewiacke River. Orange line is the water surface, and the blue line is the riverbed.

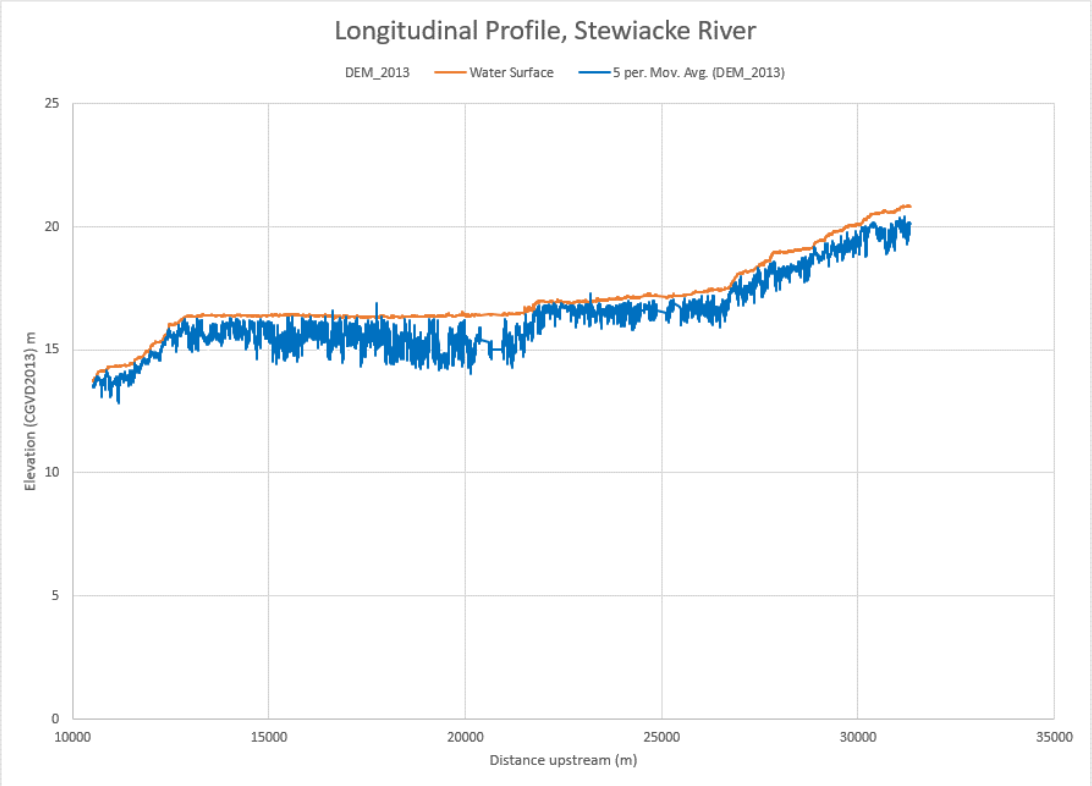

Figure 20 Close up of the long profile from upstream distance 1000 m to 3000 m. The orange line is the water surface and the blue line is the river bed.

The comparison of survey grade GPS points to the lidar DEM for hard surfaces shows and average difference in elevation of -2 cm with a standard deviation of 4 cm (Figure 21).

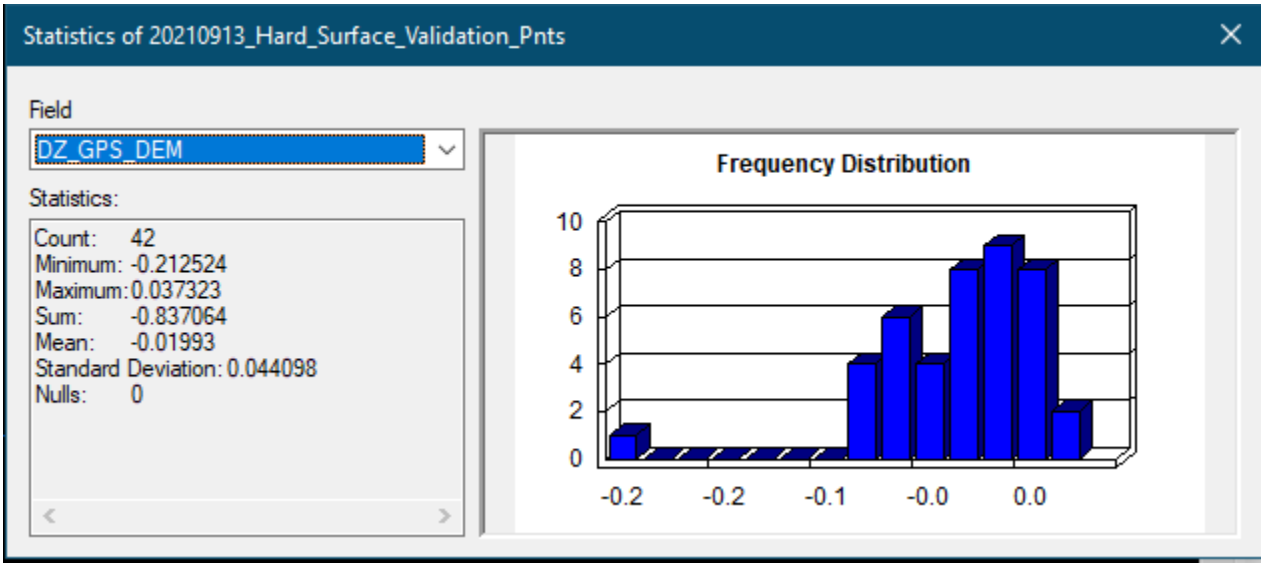

Figure 21 Histogram and statistics of the difference in elevation between the GPS points and the DEM along roads. The mean DZ (GPS-DEM) is -2 cm with a standard deviation of 4 cm.

GPS points were also collected in transects across the river where possible at two locations (Figure 22, Figure 23). In both locations the lidar DEM matches the GPS elevations very well and provides confidence in the precision of the lidar data to accurately represent the morphology and depth of the river.

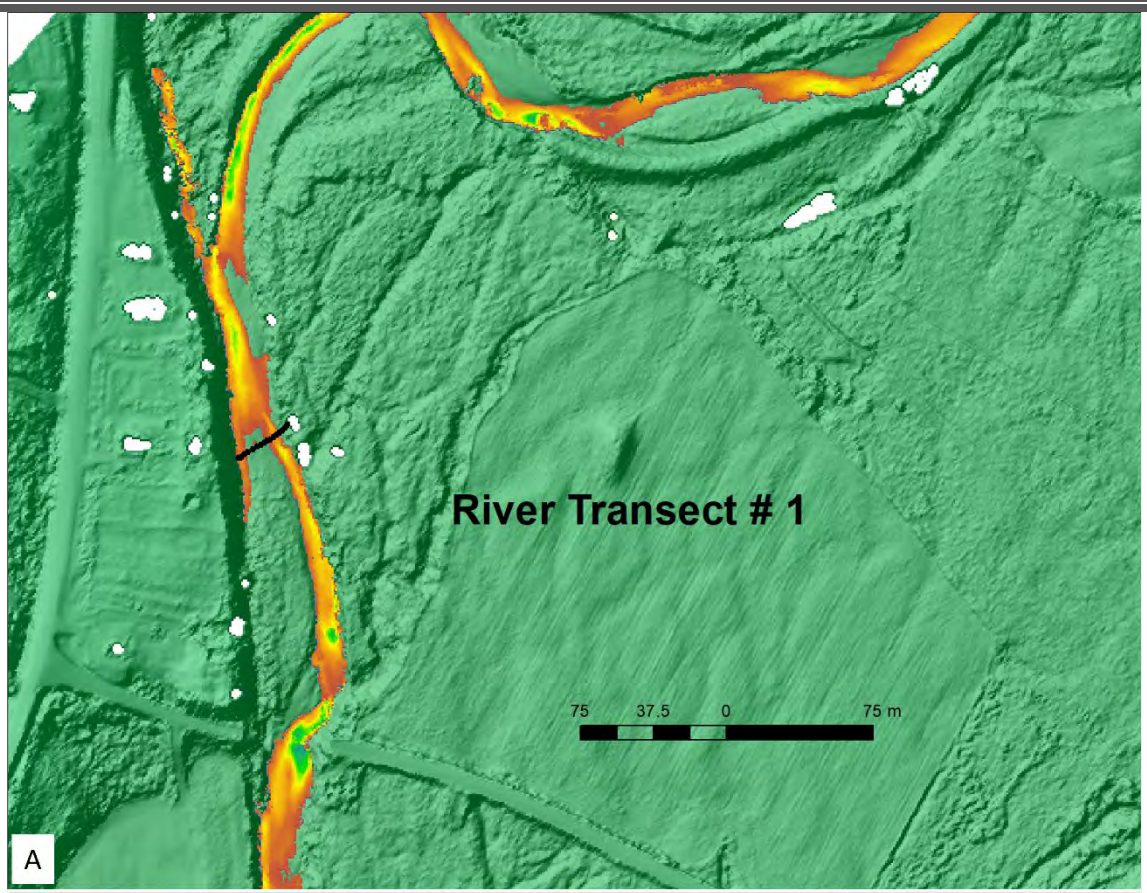

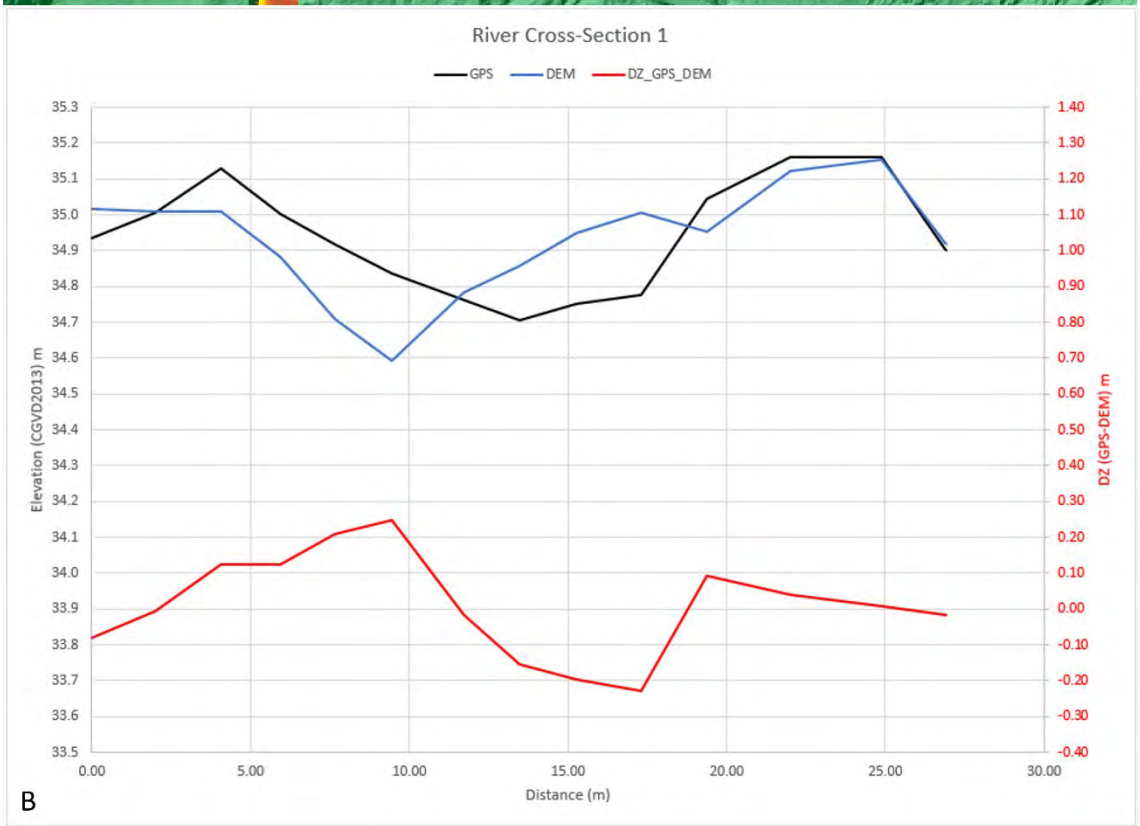

Figure 22. GPS validation of riverbed bathymetry. A) Location of transect #1. B) Graph of GPS (black) and lidar DEM (blue) with difference (GPS-DEM) in red.

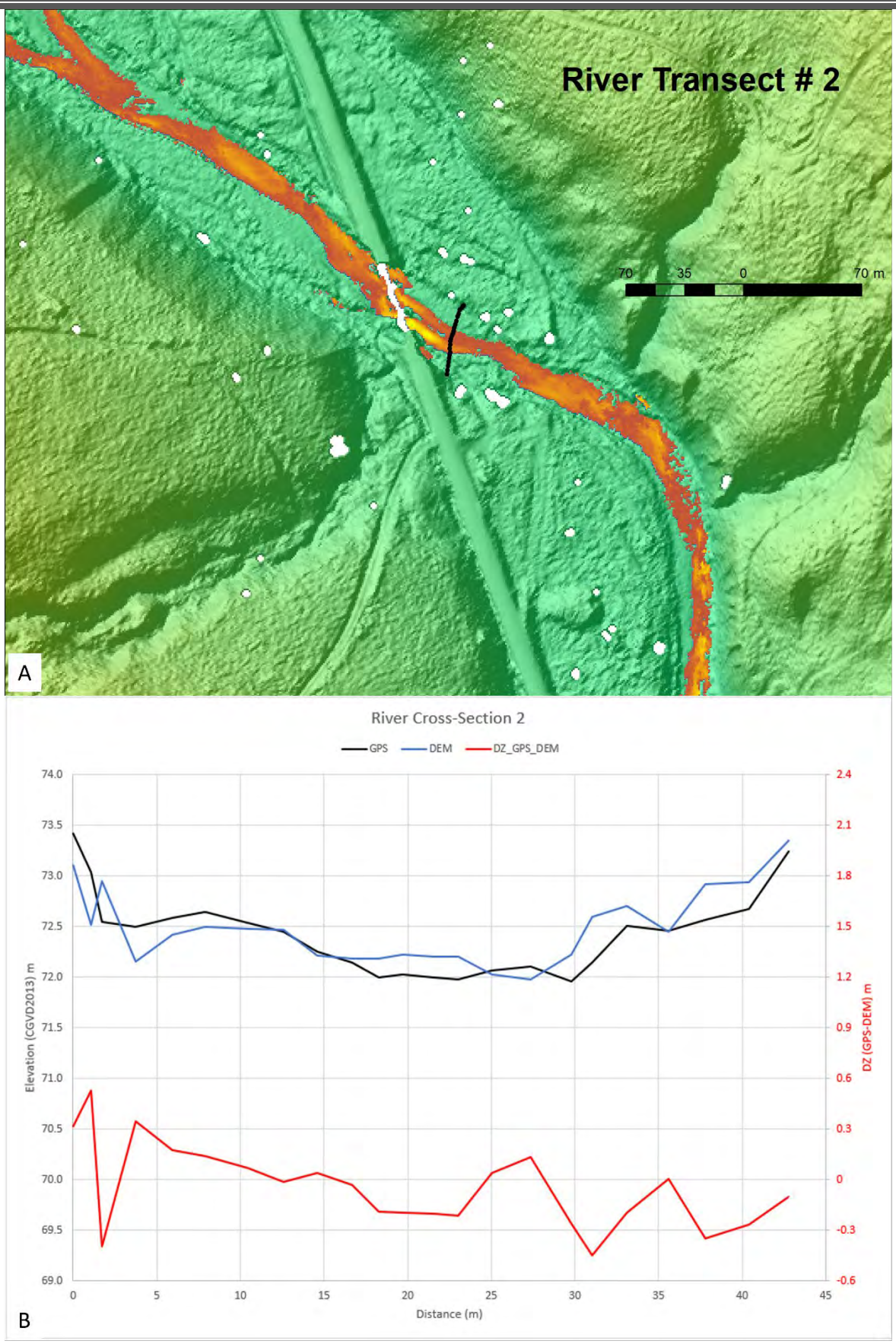

Figure 23. GPS validation of riverbed bathymetry. A) Location of transect #2. B) Graph of GPS (black) and lidar DEM (blue) with difference (GPS-DEM) in red.

The substrate mapping application is challenging in streams with relatively dark water. The lidar may penetrate to the riverbed, but the dark water can obstruct the reflected signal from the sun on the riverbed substrate. The method we have employed to attempt to map substrate utilizes both the band ratios from the RCD30 orthophotos and the water depth. When examining the substrate compared to what is observed in the riverbed from the photography and field visits, we did not attempt to classify submerged aquatic vegetation. With more research this can potentially be added to the classes that are extracted for the riverbed substrate. The results of the substrate mapping are a series of classes that are related to substrate grain size and depth, with a higher certainty for the shallow substrate types that are more distinguishable in the orthophoto imagery. The bend in the river is an example of mapping the substrate type where the riverbed is dominated by mud and sand (Figure 24). While the example farther upstream contains substrate material consisting of mud, sand and rocky sand to rock (outcrop) which form the rapids in this area (Figure 25). It should be noted that tree shadows sometime obstruct the ability to map the substrate, as is the case in these areas (Figure 24, Figure 25).

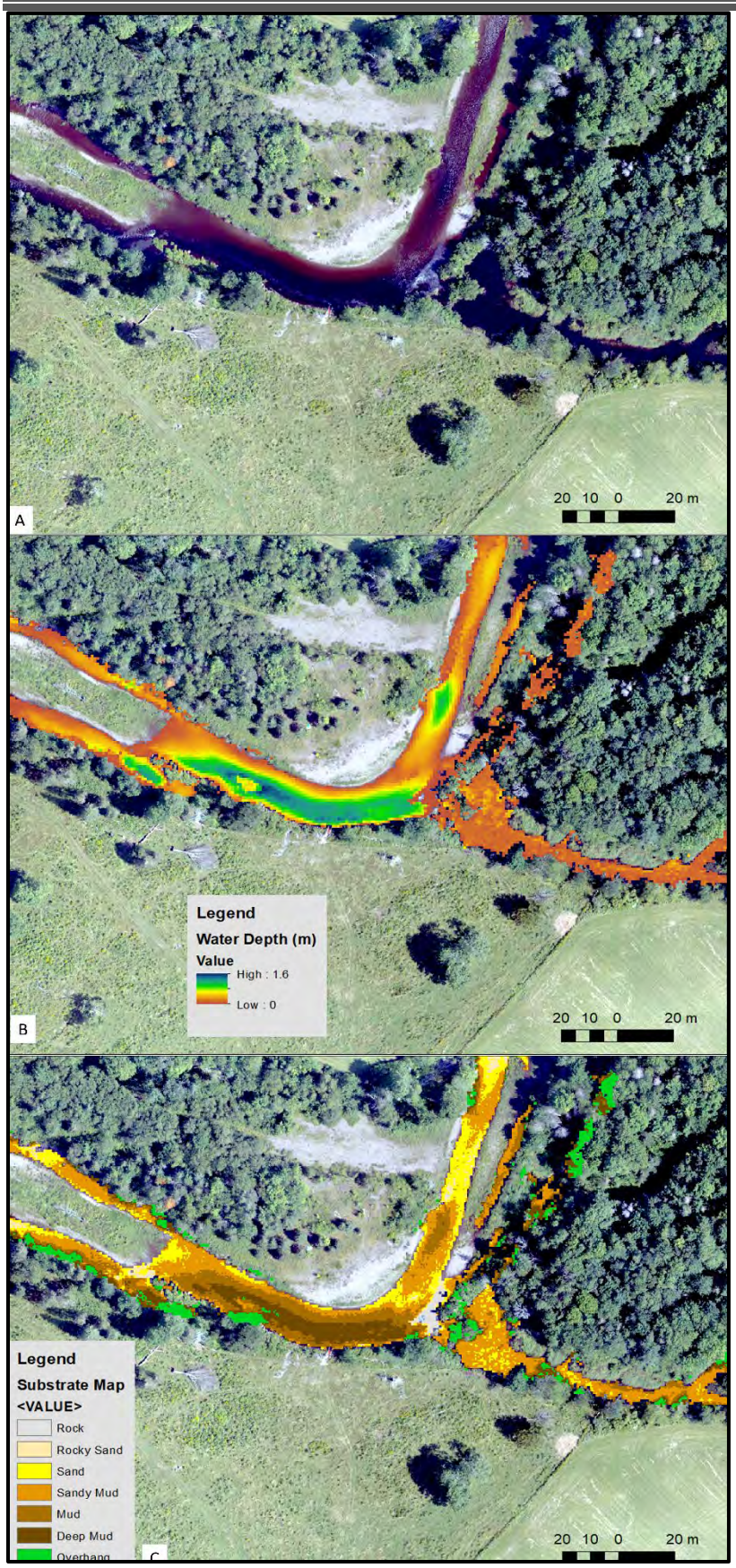

Figure 24 Example of riverbed substrate mapping. The extent of this figure is similar to that of figure 18. A) Orthophoto of river bend. B) Orthophoto with water depth. C) Substrate map of river bend.

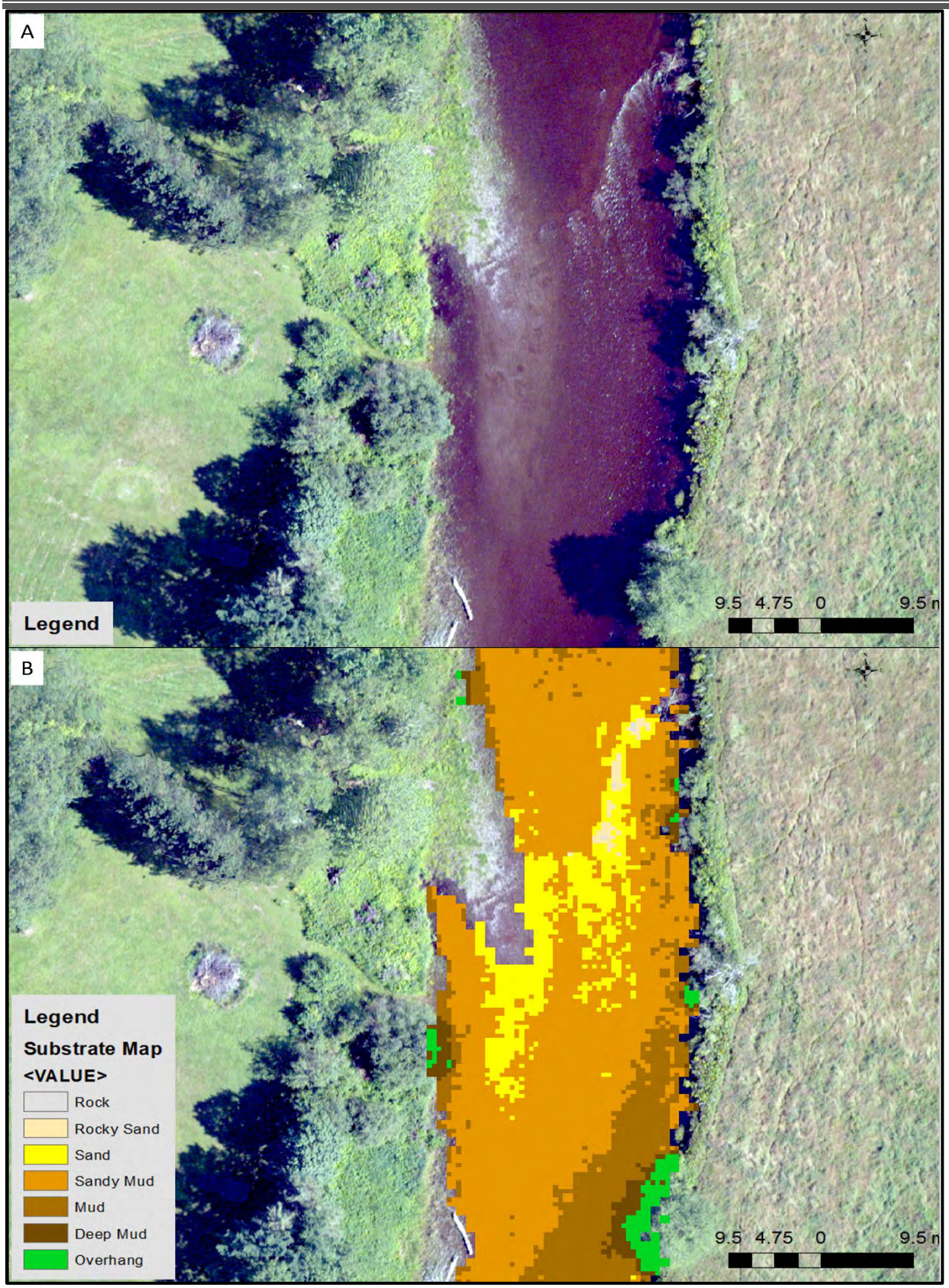

Figure 25 Another example of substrate mapping of Stewiacke Riverbed upstream of figure 24. A) Orthophoto map. B) Substrate map over orthophoto.

4 Conclusion

NSCC-AGRG surveyed the Stewiacke River in different days, Aug. 1 and Aug 18, 2022. The shape of the study area required that six different polygon areas were flown. The water clarity conditions variety quite significantly after rainfall events and both the weather and water clarity needed to be monitored to ensure a successful flight and the collection of bathymetric lidar to the riverbed. Upon inspection of the data, depths of 1.7-1.8 m were achieved. In areas of depths greater than 1.8 m the green laser signal did not appear to reach the riverbed and thus did not provide an elevation or depth for these areas. In some cases, points higher in the water column in these deep pools were misclassified as bathymetry of the riverbed. These were manually identified and marked as areas of depths > 1.8 m. In other examples where rifles occurred, the bubbles generated prevented the green laser from penetrating to the riverbed. These cases were much rarer and were identified as missing data, since the cause of misclassification was from the bubbles at the surface of the water and not a depth limitation.

The seamless DEM (including riverbed bathymetry) was subtracted from the elevations of the water surface to produce a depth map of the river. The inverse of the depth (1/Water Depth) was used to construct a “cost surface” this was used in conjunction with a start and end point along the river and the Path of Least Cost was calculated. This ensured that the path would preferentially travel through the deepest pools in the river, having the least cost. This resulted in a linear representation of the river from the start to end point. This line was used to generate a longitudinal profile, where the riverbed elevation and water surface elevation were appended to the river path along every meter of the line. The longitudinal profile was then plotted as distance upstream versus the elevation (CGVD2013) of the riverbed and water surface. This long profile highlights the overall slope of the riverbed and where pools occur along the river. It also highlights problematic areas of fish passage where the water depth is very low. We feel this GIS analysis is a useful surrogate for examining fish passage and fish habitat within the river.

We also conducted analysis to examine the river substrate. This was done utilizing the orthophoto maps where band ratios were calculated and used in combination with water depth to construct a substrate index. This index was then interpreted and used to threshold classes of substrate type. The substrate types were a combination of materials of different grain sizes at different water depths. This was our first attempt to map substrate and we had very limited ground truth data and relied on visual interpretation of the orthophoto data. It is expected with more ground truth information and testing of analytical methods that the results could improve. The substrate is important when examining fish habitat, especially when considering the riverbed material that is preferred for spanning.